

1 Fault seal modelling – the influence of fluid
2 properties on fault sealing capacity in hydrocarbon
3 and CO₂ systems

4 Rūta Karolyté^{1*}, Gareth Johnson^{2,a}, Graham Yielding³ and Stuart M.V. Gilfillan²

5 ¹ Department of Earth Sciences, University of Oxford, 3 S Parks Rd, Oxford OX1
6 3AN

7 ² School of GeoSciences, University of Edinburgh, James Hutton Road, Edinburgh,
8 EH9 3FE, UK

9 ³Badley Geoscience Ltd, North Beck House/North Beck Lane, Spilsby PE23 5NB

10 ^apresent address: Department of Civil and Environmental Engineering, University of
11 Strathclyde, James Weir Building, 75 Montrose St, Glasgow G1 1XJ

12 *Author for correspondence: ruta.karolyte@earth.ox.ac.uk

13 Keywords: fault seal; hydrocarbons; CO₂; interfacial tension; wettability; contact
14 angle; fluid properties; Otway Basin.

15 Abstract

16 Fault seal analysis is a key part of understanding the hydrocarbon trapping
17 mechanisms in the petroleum industry. Fault seal research has also been expanded
18 to CO₂-brine systems for the application to Carbon Capture and Storage (CCS). The
19 wetting properties of rock-forming minerals in the presence of hydrocarbons or CO₂
20 are a source of uncertainty in the calculations of capillary threshold pressure, which
21 defines the fault sealing capacity. Here we explore this uncertainty in a comparison
22 study between two fault-sealed fields located in the Otway Basin, south-east
23 Australia. The Katnook field in the Penola Trough is a methane field, while Boggy
24 Creek in Port Campbell contains a high-CO₂/methane mixture. Two industry
25 standard fault seal modelling methods (Yielding et al., 2010; Sperrevik et al., 2002)
26 are used to discuss their relative strengths and applicability to the CO₂ storage
27 context. We identify a range of interfacial tensions and contact angle values in the

28 hydrocarbon-water system under the conditions assumed by the Yielding et al.
29 (2010) method. Based on this, the uncertainty related to the spread in fluid
30 properties was determined to be 24% of the calculated threshold capillary pressure
31 value. We propose a methodology of threshold capillary pressure conversion from
32 hydrocarbon-brine to the CO₂-brine system, using an input of appropriate interfacial
33 tension and contact angle under reservoir conditions. The method can be used for
34 any fluid system where fluid properties are defined by these two parameters.

35 1 Introduction

36 Faults can be either pathways for, or barriers to fluid migration in the
37 subsurface and to the surface. Fault seal analytical techniques have been
38 developed to improve the prediction of hydrocarbon traps suitable for exploration.
39 More recently, fault seal research has expanded to applications to Carbon Capture
40 and Storage (CCS), where faults can act to: decrease the maximum storage
41 capacity of the reservoir; become unwanted barriers to fluid migration along the
42 planned injection pathway, causing pressure increase and limiting the maximum rate
43 of injection; or, provide a conduit for leakage of CO₂.

44 Two distinct methodologies of predictive modelling of the threshold capillary
45 pressure, which is a proxy for fault sealing capacity to hydrocarbons, have been
46 developed in the last two decades: one based on a calibration of a global dataset of
47 known sealing faults (Bretan et al., 2003; Yielding et al., 2010), and another, based
48 on laboratory measurements of fault samples (Sperrevik et al., 2002). Both of these
49 techniques have been widely applied to hydrocarbon systems. Fault capacity to seal
50 for CO₂ has been explored in theoretical studies (Iglauer, 2018; Miocic et al., 2019;
51 Naylor et al., 2010), yet there have been few attempts to test the methodology with
52 real geological examples (Bretan, 2016; Bretan et al., 2011; Yielding et al., 2011).

53 In terms of practically applying model results to either exploration of
54 hydrocarbons or CO₂ sequestration, the subject of interest is not the exact threshold
55 capillary pressure of a certain fault but rather the implications of that value to the
56 desired industrial activity. In exploration, this is applied to estimate maximum column
57 height and determine the economic viability of production. It is therefore important to
58 estimate how the uncertainty associated with the predictive method impacts the
59 prospect. In the context of CO₂ storage, threshold capillary pressure is used to

60 define the reservoir storage capacity. In this case the aim is not to overpressure the
61 fault and thus cause leakage. The practical use of fault seal modelling therefore
62 requires a good understanding of the uncertainty associated with the two different
63 approaches.

64 The interfacial tension (IFT) and the contact angle (CA) are the main fluid-
65 specific properties controlling the capillary seal and the key parameters used in both
66 hydrocarbon and CO₂ studies. The wetting properties of various rock-forming
67 minerals are different for CO₂ and hydrocarbons, which has caused a concern that
68 the seal rocks proven to retain hydrocarbon columns might be less sealing to CO₂
69 (Chiquet et al., 2007b; Daniel and Kaldi, 2009; Guariguata-Rojas and Underhill,
70 2017; Tenthorey et al., 2014). A recent study by Miodic et al. (2019) explored the
71 interplay between uncertainties in CA, IFT and fault rock composition in the CO₂-
72 brine system. The results highlighted that higher phyllosilicate content in the fault
73 rock reduces the threshold capillary pressure in the CO₂-brine system due to the
74 wettability of the clay minerals in the presence of CO₂, especially at depths > 1 km.

75 Our understanding of CA and IFT primarily relies on empirical
76 measurements, meaning that significant uncertainty exists in both hydrocarbon and
77 CO₂-brine systems. While the above concerns are valid for the CO₂ storage, the
78 existing uncertainties associated with CA and IFT also exist in the hydrocarbons.
79 This is because of the wide range of chemical compositions of crude oil and the
80 difficulty of sampling undegassed reservoir fluids.

81 In this contribution we investigate the uncertainty associated with the fluid
82 properties (CA, IFT) as well as geological assumptions required for the model (depth
83 at the time of faulting and maximum burial depth) in two field examples. One,
84 methane gas field in South Australia (Katnook), and another, a high CO₂/methane
85 mixture in Port Campbell, Victoria (Boggy Creek). In both cases, a gas column is
86 supported by the fault rock and the column height is known. The fields are located in
87 the Otway Basin, which is very well characterised in respect to hydrocarbon
88 exploration as well as CO₂ storage. These case studies therefore provide a realistic
89 example of the level of uncertainties that can be expected in future potential CO₂
90 storage sites.

91 This approach allows us to verify if the model predictions are valid and
92 systematically compare the uncertainties in the CO₂ and methane system. Fault seal
93 analysis is performed using the Sperrevik et al. (2002) and Yielding et al. (2010)
94 fault seal modelling methods. The objective is to discuss the differences in the
95 modelling approaches, their associated uncertainties and suitability for the CO₂-
96 brine system. The former method inherently allows the conversion from mercury-air
97 system to CO₂-brine, while the latter method is calibrated to a hydrocarbon system.
98 We summarise the current understanding of the IFT and CA ranges in hydrocarbons
99 that the Yielding et al. (2010) method is based on to define the expected IFT and CA
100 distribution and their mean values. Based on this, we propose a new calibration of
101 the Yielding et al. (2010) algorithm to the CO₂-brine system.

102 2 Fault rock seal dependencies

103 Fault rock seals occur when movement along a fault plane creates a low-
104 permeability fault rock, and depend on the fault rock composition as well as the
105 properties of the fluids in the system. In siliciclastic sand-shale sequences, the
106 sealing fault rocks are characterised by continuous clay-rich smears (Lindsay et al.,
107 1993). Their thickness is favoured by greater thickness of shale beds in host rocks,
108 weight of the overburden, and burial depth (Lehner and Pilaar, 1997). Quartz
109 cementation at temperatures above 90 °C or ~>3 km further decreases fault rock
110 porosity and increases the sealing potential (Fisher and Knipe, 1998; Rimstidt and
111 Barnes, 1980). The resulting fault rock may act as baffle to fluid migration through a
112 process of capillary sealing, which is created by the opposing forces between the
113 two phases at their interface – the wetting phase (water or brine) and the non-
114 wetting phase (hydrocarbons or CO₂, in this context) (Fisher and Knipe, 1998;
115 Watts, 1987; Yielding et al., 1997). Capillary seals fail when the fluid buoyancy
116 pressure exceeds the threshold capillary pressure. Capillary threshold pressure (P_c)
117 is therefore a key fault rock attribute used in the hydrocarbon exploration industry to
118 determine the sealing potential of the fault and calculate maximum column heights
119 (h_{max}), using the relationship between the height of the fluid column and the
120 buoyancy pressure it exerts on the sealing rocks (Schowalter, 1974):

$$121 \quad P_c = \frac{2IFT \times \cos\theta}{r} \quad (1)$$

122
$$h_{max} = \frac{P_c}{(\rho_h - \rho_w)g} \quad (2)$$

123 Where IFT is the interfacial tension between the fluids, θ is the contact
124 angle, r is the effective pore throat radius, ρ is density, g is acceleration due to
125 gravity, h and w denote hydrocarbons and water.

126 The interfacial tension and contact angle (or wettability) are the key
127 properties controlling capillary seal and depend on many factors including pressure,
128 temperature, fluid type, fluid density and rock mineralogy (e.g. Iglaue et al., 2015;
129 Nordgard Bolas et al., 2005; Øren and Bakke, 2003; Radke et al., 1992; Schowalter,
130 1974). The influence of these factors is a key concern in describing fault zone
131 behaviour. The advantage, however, is that the characteristics of fluids and their
132 affinity to reservoir rock can be approximated by these two input parameters, and
133 therefore applied in the same manner to systems involving hydrocarbons, CO₂ or
134 any other fluid type of interest.

135 The buoyancy pressure exerted on the fault rock by the column of fluid is
136 greater with increasing density contrast between the wetting and the non-wetting
137 phases. Under typical reservoir conditions, density of methane ranges between 100
138 – 300 kg/m³, CO₂ is approximately 400 – 600 kg/m³ and oil density varies between
139 700 – 1000 kg/m³ (Danesh, 1998). Brine density depends on salinity and has a
140 value of 1000-1150 kg/m³. It is therefore apparent, that a fault rock with a certain
141 capillary threshold pressure would retain a smaller column of methane than of CO₂
142 or oil, if the other parameters were the same. However, the differences in interfacial
143 tension and CA between CO₂ and hydrocarbons also impact the threshold capillary
144 pressure of the fault rock in a CO₂-brine system (Chiquet et al., 2007b). The
145 interplay between IFT, CA and fluid density therefore is key to consider in applying
146 fault seal modelling techniques to CO₂ sequestration.

147 The effective pore throat radius of a fault zone is impossible to directly
148 determine, and by standard practice is approximated using a predictive algorithm
149 based on the clay content of the faulted rocks. Examples include Clay Smear
150 Potential (CSP) (Bouvier et al., 1989; Fulljames et al., 1997), Shale Smear Factor
151 (SSF) (Lindsay et al., 1993) and Shale Gouge Ratio (SGR) (Yielding et al., 1997).
152 We use SGR in this study due to its direct calibration to threshold capillary
153 pressures and, in turn, gas column heights.

154 Two different approaches have been developed to link SGR to capillary
155 threshold pressure. One approach is based on laboratory experiments of mercury-
156 air injection tests in micro-fault samples and subsequent correlation of measured
157 capillary pressures to sample clay content (Sperrevik et al., 2002), based on earlier
158 studies by Knipe (1997), Gibson (1998). The second approach uses data from
159 known hydrocarbon traps sealed by faults to empirically correlate the maximum
160 observed buoyancy pressures (assumed equivalent to threshold pressure) to SGR
161 values (Bretan et al., 2003; Yielding, 2002; Yielding et al., 2010). The two
162 approaches have been termed 'deterministic' and 'empirical' respectively (Yielding
163 et al., 2010), and will be referred to as such in the forthcoming text. The two
164 methods are often used in conjunction and have been shown to produce similar
165 results in certain but not all SGR/burial depth configurations (Yielding et al., 2010).
166 To date, the application of these methods to the CO₂-brine systems has been limited
167 (Bretan et al., 2011).

168 The deterministic approach is based on laboratory measurements of fault
169 rock permeability from a variety of fault structures within reservoir core samples and
170 requires a conversion from the mercury-air system to hydrocarbon-water or CO₂-
171 brine system by using appropriate values for IFT and contact angle between the
172 fluid and the wetting phase (Sperrevik et al., 2002). In contrast, the empirical
173 approach (Bretan et al., 2003; Yielding, 2002) is based on a calibration of SGR
174 values and across-fault buoyancy pressure differences of known sealing faults.
175 Importantly, the calibration includes only hydrocarbons at depths greater than 1.5
176 km. This means that theoretically, the method can only be applied to fluid systems
177 which fall within the range of IFT and contact angle parameters as the hydrocarbon
178 field used in the calibration. Further constraining this range is discussed below
179 before we propose a methodology to convert fault seal modelling results from
180 hydrocarbons to CO₂-brine system.

181 3 Geological background

182 In this study we describe two gas fields in the Otway Basin, Victoria, Australia: The
183 Katnook field in the Penola Trough and the Boggy Creek field in the Port Campbell
184 embayment. Below we outline the geology of the fields in terms of stratigraphy, trap
185 geometries and gas charge.

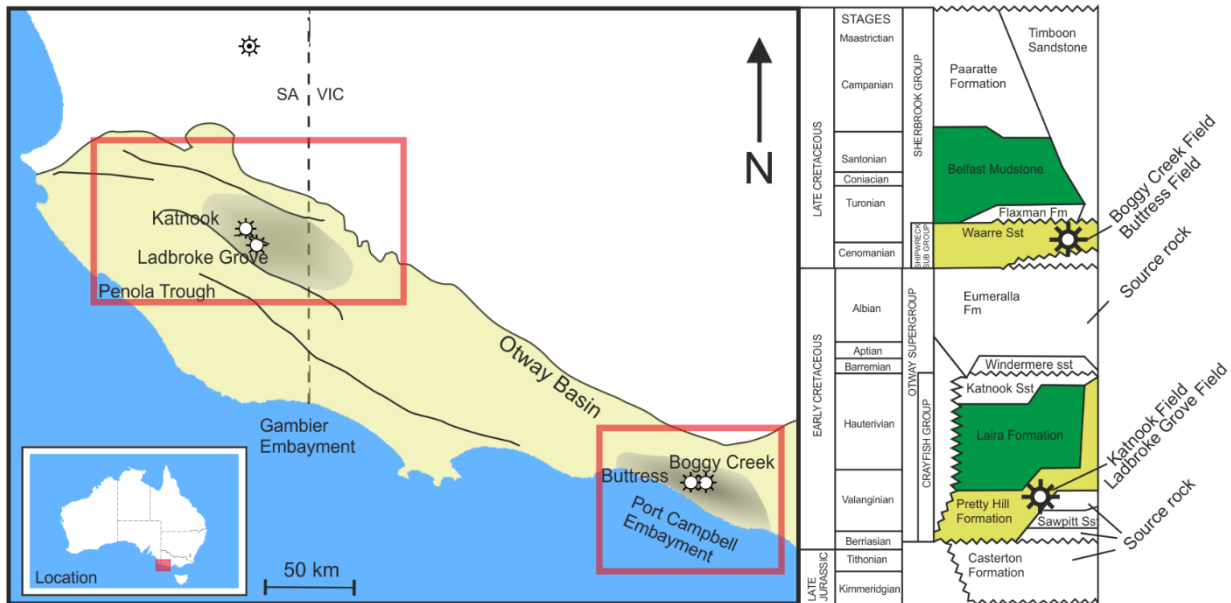
3.1 Basin stratigraphy

187 The present day geometry of the Otway Basin was developed during the
188 Cretaceous to Miocene rifting with a period of inversion in the mid-Cretaceous, when
189 the rift axis moved south (Teasdale et al., 2003). A series of graben and half-graben
190 structures consist of compartmentalised fault-bound reservoirs, with numerous
191 hydrocarbon and CO₂ accumulations (Fig. 1). Two case studies discussed here
192 present examples of gas column retention by a fault rock in a situation of reservoir-
193 reservoir juxtaposition. Katnook in the Penola Trough is a methane field, while the
194 Boggy Creek field in Port Campbell contains a high-CO₂/methane mixture.

195 The two fields are within different reservoir formations at different
196 stratigraphic intervals (Fig. 1). The Katnook field is stratigraphically lower, located in
197 Pretty Hill Formation of 2 - 4.5 km thickness, within the Pretty Hill Sandstone. The
198 main target reservoir is the Pretty Hill Sandstone member at the top of the sequence
199 (Lyon et al., 2005). The formation consists of massive, slumped and cross-bedded
200 sand packages, classified as lith-arenites to feldspathic lith-arenites, deposited in
201 continental fluvio-lacustrine environment (Little and Phillips, 1995). The Laira
202 Formation forms a regional seal, comprised of siltstones and shales interbedded
203 with sandstones. The Katnook sandstone at the top of the Crayfish Group
204 (consisting of both the reservoir and the seal lithologies) is also gas-bearing, but is
205 not a subject to this discussion. Katnook-1 and 2 are production wells targeting
206 Katnook sandstone within the Crayfish Group, while Katnook-3 produces from the
207 deeper Pretty Hill Formation. Shale units within the lower parts of the Pretty Hill
208 Formation and the underlying Casterton Formation are the oil and gas source rocks
209 in the Penola Trough and the SW part of the basin (Boreham et al., 2004).

210 The Boggy Creek CO₂ field is stratigraphically higher, within the Waarre
211 Sandstone, comprised of deltaic and shallow marine interbedded siltstones and
212 shales, segregated into four units defined by depositional environments. Unit C, the
213 main reservoir interval, is poorly sorted, medium to coarse-grained quartz arenite
214 (Watson et al., 2004). The underlying Eumeralla Formation consist of inter-bedded
215 lithic sandstones, siltstones, coals and claystones (Cockshell et al., 1995). The
216 deeper coal-rich units of Eumeralla Formation are the source rocks in the SE part of
217 the basin. The Belfast Mudstone overlies the reservoir and forms a regional seal
218 (Boreham et al., 2004).

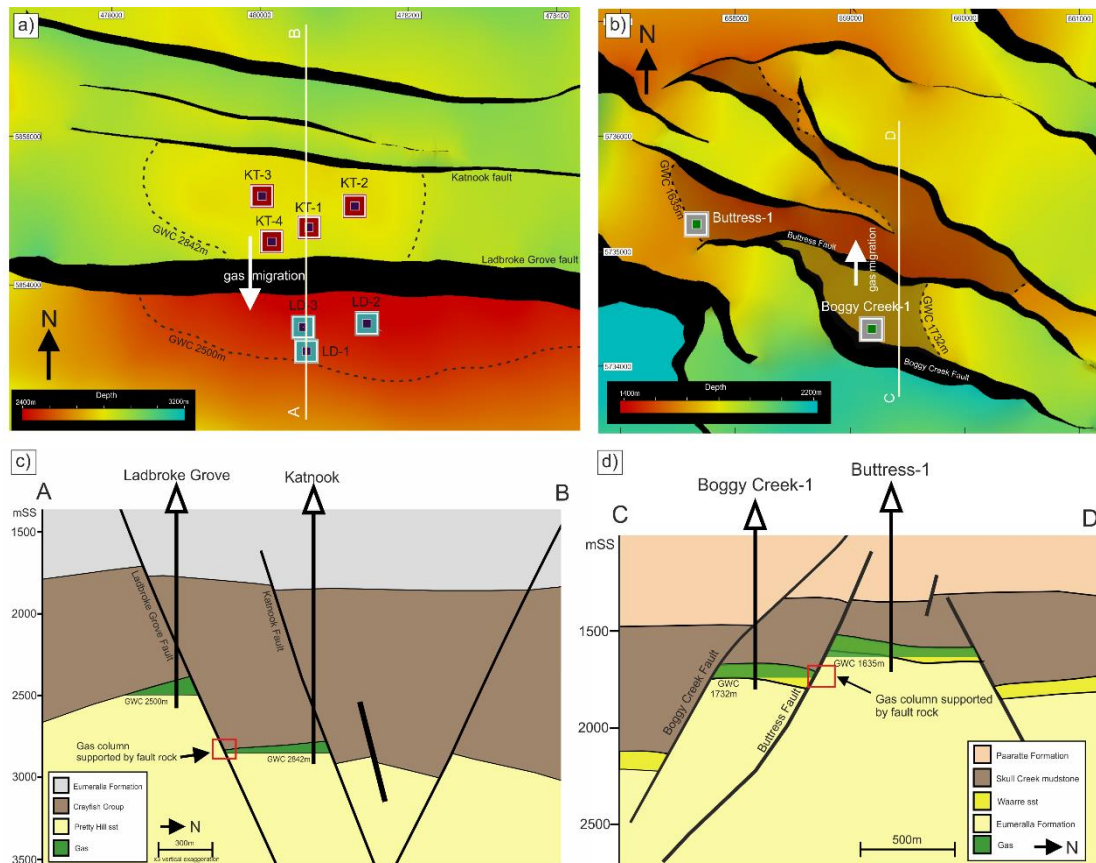
219 The Waarre sandstone is approx. 90 m thick and the main producing interval
 220 within it (Unit C) is 25 -40 m thick (Dance, 2013). The underlying Eumeralla
 221 Formation is up to 3 km thick (Cockshell et al., 1995). Significant oil shows have
 222 been observed within the Eumeralla Formation in other parts of the basin (Lisk,
 223 2004) and therefore good connectivity between the Waarre and Eumeralla units is
 224 expected despite the silt and clay inter-beds.



225
 226 *Figure 1. Location map of Penola Trough (Katnook/Ladbrooke Grove fields) and Port*
 227 *Campbell (Buttress/Boggy Creek fields). Both localities are within the Otway Basin. Inset on*
 228 *the right shows the location of both reservoirs within the stratigraphic column (adapted from*
 229 *Lyon et al., 2004).*
 230

231 3.2 Trap geometry

232 The Katnook field is bound by the Katnook fault to the north and Ladbrooke
 233 Grove fault to the south (Fig. 2a). The northern side of the field is juxtaposition-
 234 sealed against Crayfish Group shales, while the southern side reaches the Ladbrooke
 235 Grove Fault, where the reservoir is self-juxtaposed (Fig. 2c). The fault rock supports
 236 a column of 31 m on the southern edge of the gas field; the total gas column height
 237 is 101 m. The Boggy Creek field is bound by the Boggy Creek Fault to the south and
 238 the Buttress Fault to the north (Fig. 2b). Similarly to the Katnook field, the main seal
 239 to the reservoir is provided by juxtaposition seal to the south (total gas column 128
 240 m), but fault rock seal exists to the north, supporting a gas column of 51 m (Fig. 2d).



241
 242 *Figure 2. Map and cross-sectional views of Penola Trough (a, c) and Port Campbell (c, d)*
 243 *gas field locations. a) Map view of the top of the Pretty Hill reservoir horizon, coloured by*
 244 *depth. b) Map view of the top of the Waarre sandstone reservoir horizon, coloured by*
 245 *depth. c) Cross-section view of line A-B from figure (a). Ladbrooke Grove and Katnook fields in*
 246 *Penola Trough. Cross-section drawn from seismic data using 3x vertical exaggeration.*
 247 *Katnook field is supported by Katnook fault to the north (juxtaposition seal) and Ladbrooke*
 248 *Grove fault to the south (fault rock seal). d) C-D cross-section view (from figure b) of the*
 249 *Boggy Creek and Buttress fields in Port Campbell. Cross-section drawn from seismic data*
 250 *without vertical exaggeration. Boggy Creek gas field is retained by juxtaposition seal to the*
 251 *south and fault rock seal to the north. The adjacent Buttress field is structurally higher. Cross*
 252 *sections created using 3D Balnaves-Haselgrove seismic survey (Lyon et al., 2004) (c) and a*
 253 *combination of OGF93A, ONH01 and Curdie Vale 3D seismic surveys (Ziesch et al., 2017)*
 254 *(d).*

255 3.3 The sequence of gas charge events

256 The two main phases of hydrocarbon generation in the Otway Basin are
 257 estimated at mid-Cretaceous (Boult et al., 2004) and mid-Paleogene (Duddy, 1997),
 258 based on thermal maturation modelling and the relationship between GWC positions
 259 above spill points and known gas diffusion rates (Lyon et al., 2005). Early oil/wet gas
 260 charge was flushed or diluted by later dry gas charge (Boreham et al., 2004).
 261 Methane charge was followed by a later stage magmatic CO₂ injection (Chivas et
 262 al., 1987; Lyon et al., 2005; Watson et al., 2003). Due to the sealing or partially

263 sealing nature of bounding faults, the CO₂/methane ratio significantly varies across
264 geographically closely located fields.

265 The Ladbroke Grove field contains CO₂, with higher concentrations at the
266 base (49%) and lower at the top of the reservoir interval (27%). The Katnook field
267 contains primarily methane with only trace amounts of CO₂ (0.2%). ³He/⁴He,
268 CO₂/³He and neon isotopic ratios indicate that CO₂ in Ladbroke Grove is of mantle
269 origin (³He/⁴He = 1.46 R/R_A) (Karolytè, 2018). ³He/⁴He ratios in the Katnook field are
270 slightly elevated above the crustal values (0.06 R/R_A), but any mantle-sourced noble
271 gases are decoupled from the migrating CO₂ (Karolytè, 2018). The geochemistry
272 results suggest that CO₂ charge was restricted to the Ladbroke Grove field and did
273 not pass through the Katnook field. The spill-point in the Katnook field would lead to
274 charging the Balnaves trap, which does not contain a live column (Lyon et al., 2015).
275 The presence of a fault-rock supported column and column absence in the Balnaves
276 field suggest that methane was likely charged to the Ladbroke Grove field through
277 failure of fault capillary seal, however separate charge events cannot be discounted.

278 The Boggy Creek and Buttress fields both contain mixtures of mantle CO₂
279 and methane. CO₂ concentrations within the traps increase with depth because of
280 its higher density, and Boggy Creek (87% CO₂) is more CO₂-rich than Buttress (77%
281 CO₂) (Karolytè et al., 2019). The observed concentration gradient suggests that CO₂
282 was first charged to the Boggy Creek field, and later migrated to Buttress, and more
283 methane at the top of the formation was lost relative to CO₂, however, independent
284 charge to both fields cannot be completely excluded.

285

286 4 Methods

287 4.1 Geological 3D models

288 This work has been undertaken using a compilation of existing industry and
289 academic datasets. 3D model development, structural and fault seal analysis was
290 undertaken using TrapTester™ software. The Penola Trough 3D model was
291 developed by Paul Lyon and published in Lyon et al. (2005b, 2007, 2004). It was
292 constructed by interpretation of the 3D Balnaves-Haselgrove seismic survey in time

293 and pseudo-depth (Lyon et al., 2004). The 3D model used for Port Campbell area
294 was developed by Ziesch et al. (2017) using a combination of OGF93A, ONH01 and
295 Curdie Vale 3D seismic surveys. Seismic data reinterpretation in this study has led
296 to addition of some new faults and modification of fault and horizon geometries in
297 the original models.

298 4.1.1 V-shale

299 The V-shale curves for the studied wells were created from GR wireline logs.
300 'Clean sand' and 'pure shale' (0 and 100% V-shale) values were determined by
301 correlating GR measurements to core descriptions and, where possible, core
302 permeability tests from the well completion reports. The Waarre sandstone is
303 feldspathic (Watson et al., 2003), which is reflected in the relatively high chosen API
304 (American Petroleum Institute unit) values of clean sands. The strength of the GR
305 signal is often not uniform between different wells, in which case different clean
306 sand and pure shale values have to be chosen to produce internally consistent V-
307 shale logs. The V-shale values were calculated using the linear response equation
308 (Asquith et al., 2004):

$$309 \quad V_{Shale} = I_{GR} = \frac{GR_{log} - GR_{sand}}{GR_{shale} - GR_{sand}} \quad (3)$$

310 Multiple V-shale curves were used to project an average V-shale profile on
311 the fault plane. Six well logs were used on the Ladbroke Grove fault (LD-1, LD-2,
312 LD-3, JT-1, KT-2, KT-3) and two on the Buttress fault (Buttress-1, Boggy Creek-1).

313 **4.1.2 Fault seal modelling**

314 The intersection lines between the top of the reservoir formation on the
315 footwall and the hanging wall side of the fault were created on the fault planes (e.g.
316 Yielding & Freeman, 2016). Manual quality check techniques such as projecting
317 seismic slices on the fault plane were used to accurately map out the geometry of
318 the intersections. Allan diagrams (Allan, 1989) were created to identify the areas of
319 interest where reservoir formation is juxtaposed against another permeable rock on
320 the other side of the fault.

321 Buoyancy pressure is calculated on the 3D surface of the fault based on the
322 input of gas water contact (GWC) and gas pressure gradient (Appendix 2), which is
323 dependent on the fluid density. Gas densities at reservoir conditions for the
324 particular gas mixtures were calculated using the Peng-Robinson equation of state
325 (Peng and Robinson, 1976). The pressure data were obtained from repeat formation
326 tester (RFT) plots in well completion reports (WCRs) from Buttress and Ladbrooke
327 Grove fields. Pressure profile data did not exist for Katnook and Boggy Creek fields,
328 so gas pressure gradients were calculated from gas densities. A summary of input
329 parameters relevant to buoyancy pressure calculation is given in Table 1.

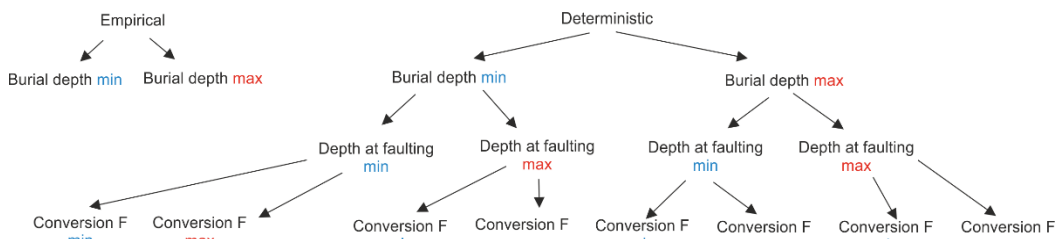
330
331
332
333

Table 1. Summary of parameters used in the buoyancy pressure calculations. Temperature and pressure relevant where density was calculated using equation of state rather than obtained from RFT measurements. Major gas compositions are from Karolytė (2018) and Karolytė et al. (2019).

Field	Temperature °C	Pressure MPa	GWC mSS	ρ_w kg/m ³	ρ_g kg/m ³	Major gas composition		
						C ₁₊	N ₂	CO ₂
<i>Penola Trough</i>								
Ladbroke Grove	104	23	2500	927	244	45	7.2	49
Katnook	118	28	2842	1035	125	97	3.2	0.2
<i>Port Campbell</i>								
Buttress	62	16	1635	1035	382	22	1.9	77
Boggy Creek	59	17	1732	1035	456	10	2.0	87

336

337 SGR was calculated on the 3D plane of the fault using the input of V-shale
338 curves using the Yielding et al. (1997) method. The threshold capillary pressures
339 were calculated using two different SGR calibration techniques: empirical (Yielding
340 et al., 2002; Yielding et al., 2010) and deterministic (Sperrevik et al., 2002) (detailed
341 methods available in Appendix 1). Both of these methods require an input of the
342 maximum burial depth. The empirical method uses the burial depth to categorize
343 faults for three different seal envelopes (< 3 km, 3 - 3.5 km, 3.5 – 5 km), while the
344 deterministic method directly incorporates the value. The deterministic method
345 additionally requires an estimate of the depth at the time of faulting and a conversion
346 factor from mercury-air to gas-brine system, which is dependent on the interfacial
347 tension between the wetting and non-wetting phases and the wettability of the
348 system. A minimum and maximum estimate of each of the parameters were
349 determined based on known reservoir conditions and a literature review, resulting in
350 two and eight possible scenarios for the empirical and deterministic methods,
351 respectively (Fig. 3). Both of these methods ascribe threshold capillary pressures to
352 every point of the 3D fault surface. These can then be compared to the known
353 buoyancy pressure exerted by the gas column trapped in the reservoir.



354
355
356

Figure 3. Schematic diagram of different scenarios including minimum and maximum estimates of parameters required by the empirical and deterministic methods.

357 **4.1.3 Input parameters**

358 The input parameters used in the fault seal modelling are summarised in
 359 Table 2, and the reasoning is explained below.

360 **Table 2. Summary of parameters used in fault seal modelling**

Field	Burial depth (m) (for deterministic)		Burial depth (m) (for empirical)		Depth at the time of faulting (m)		Conversion factor	
	min	max	min	max	min	max	min	max
Boggy Creek	1623	1783	<3000	-	450	1200	0.054	0.087
Katnook	2787	2987	<3000	3000-3500	800	1200	0.111	0.133

361
362

363 **4.1.3.1 Maximum burial depth**

364 The Otway Basin has undergone two significant phases of uplift and
 365 denudation, but the effects are less significant at the margins of the basin where the
 366 two case studies are situated. A comprehensive basin-wide sonic transit time study
 367 by (Tassone et al., 2014) suggests that Port Campbell is close to its maximum burial
 368 depth, with a net exhumation range obtained from Boggy Creek-1 indicating 0 – 160
 369 m net exhumation. The same is true for Penola Trough, where conservative
 370 estimate of net exhumation is in the range of 0 - 200 m. This is confirmed by vitrinite
 371 reflectance and apatite fission track data (Boult and Hibburt, 2002; Duddy, 1997).
 372 The upper end of this range gives a maximum burial depth of 2987 m, which is very
 373 close to the cut-off value of 3 km between different seal envelopes in Yielding et al.
 374 (2010) method. We therefore consider two scenarios of < 3 km and 3 - 3.5 km
 375 maximum burial depth for the Penola Trough.

376 **4.1.3.2 Depth at the time of faulting**

377 **4.1.3.2.1 Penola Trough**

378 The main faulting event was contemporaneous with the Early Cretaceous
 379 rifting which coincided with the deposition of the regional seal formation. The
 380 sediments of the Crayfish Group commonly drape over major structural highs,
 381 indicating that faulting had ceased by the end of its deposition (Briguglio et al., 2015)
 382 and was inactive during the deposition of the overlying Eumeralla Formation (Boult
 383 et al., 2008), which is also evident from the seismic data. The depth of Ladbroke

384 Grove fault at the time of displacement is therefore constrained by the total
385 thickness of the Crayfish Group. The current thickness of the Crayfish Group in the
386 Katnook well is 800 m, which is also the thickest in the Penola Graben. Structural
387 cross-section balance and restoration indicates that 400 m of Crayfish sediments
388 were removed in the Penola Graben (Briguglio et al., 2015). Depth at the time of
389 faulting is therefore constrained to 800 - 1200 m.

390 **4.1.3.2 Port Campbell**

391 The seal formation, consisting of a succession of mudstones overlain by
392 Skull Creek mudstone, varies in thickness across the faults, indicating syn-
393 sedimentary faulting (Ziesch et al., 2015). The faulting ceased during the deposition
394 of the unconformably overlain Wangerrip Group in Paleocene. Depth at the time of
395 faulting is therefore represented by the thickness of this group, which ranges from
396 450 to 1200 m.

397 **4.1.4 Conversion factor**

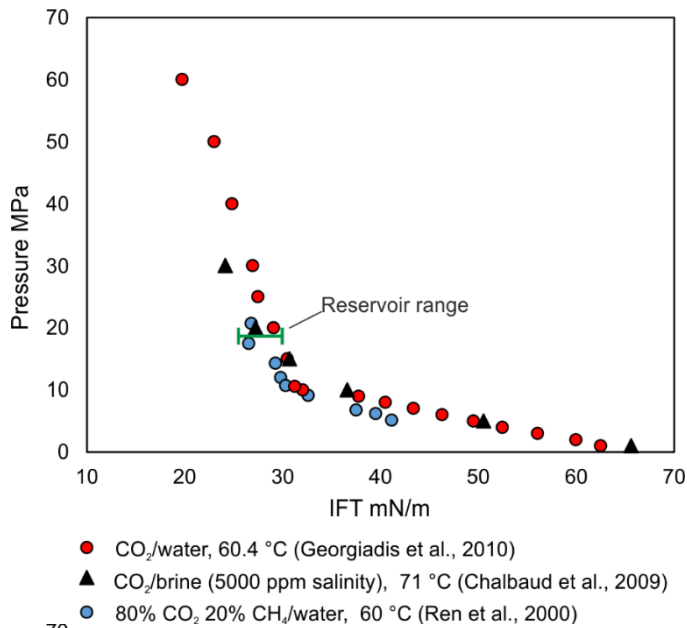
398 The conversion factor from mercury-air to the chosen wetting and non-
399 wetting phase requires an input of IFT and contact angle:

$$400 \quad P_{wn} = P_{ma} \times \frac{IFT_{wn} \times \cos\theta_{wn}}{IFT_{ma} \times \cos\theta_{ma}} \quad (4)$$

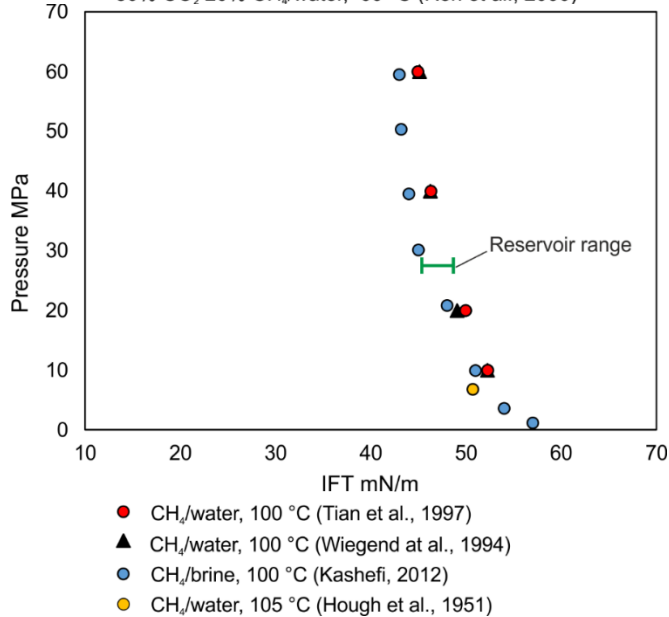
401 where P is threshold capillary pressure, θ is the contact angle, wn and ma denote
402 wetting/non-wetting phase of choice and mercury/air, respectively. The air-mercury
403 IFT and CA are 480 mN/m and 140°, respectively (Vavra et al., 1992).

404 IFT has a strong dependency on pressure and temperature for both CO₂
405 and methane, so assessment for local reservoir conditions is imperative. Figure 4
406 shows a compilation of results selected from laboratory studies under conditions
407 similar to those in Boggy Creek and Katnook reservoirs. Presented data include
408 CH₄-water, CO₂-water, CO₂-brine and CO₂-CH₄ mixtures in water (Chalbaud et al.,
409 2009; Georgiadis et al., 2010; Hough et al., 1951; Kashefi, 2012; Ren et al., 2000;
410 Wiegand and Franck, 1994; Yi-Ling et al., 1997). The range constrained for the
411 Boggy Creek field is 26 - 32 mN/m (Fig. 4). Admixture of CH₄ to pure CO₂ generally
412 increases the IFT, but as shown in Figure 4a, the measurements in mixtures
413 containing < 20% methane are not significantly different from CO₂-water system

414 (Ren et al., 2000). The IFT range expected in Katnook methane field is 47-49 mN/m
 415 (Fig. 4b).



416



417
 418 *Fig. 4. IFT vs pressure for a) Boggy Creek reservoir conditions b) Katnook reservoir*
 419 *conditions. Green line shows the expected range for reservoir pressure.*
 420

421 Typical reservoir rocks are often considered to be water-wet in the presence
 422 of hydrocarbons (e.g. Schowalter, 1974; Vavra et al., 1992), with some exceptions,
 423 including grain coating with high polarity of crude oil components (Singh et al.,
 424 2016). The Penola Trough traps show evidence for early charge of oil which was
 425 later displaced by gas (Higgs et al., 2015; Lovibond et al., 1995), therefore a range

426 of 0-30° contact angles is taken to reflect the potential effect of acid adsorption on
427 grain surfaces.

428 The wettability of CO₂-brine-mineral system has been investigated by a
429 growing number of studies (Bikkina, 2011; Farokhpour et al., 2013; Jung and Wan,
430 2012), most commonly directly on single mineral surfaces, where minerals are
431 required to be ultraclean and smooth on an atomic level for reproducible results. The
432 results are highly variable (0 - 90°), but much of the variation is attributed to the
433 surface roughness and sample preparation practices (Iglauer et al., 2015). However,
434 the most consistent findings include a contact angle increase by up to 30° at CO₂
435 transition from the gaseous to the supercritical phase (Jung and Wan, 2012;
436 Sutjiadi-Sia et al., 2008). Recent core-flooding experiments show that water-wet
437 reservoir conditions do not change during prolonged exposure to supercritical CO₂
438 (Garing et al., 2019). In the absence of minerals known to be particularly
439 hydrophobic in the presence of CO₂ in the reservoir, the expected contact angle
440 range for Boggy Creek is taken to be 10 - 40°, as expected for common silicate and
441 carbonate reservoir minerals (Espinoza and Santamarina, 2010).

442 Given the defined range of IFT and contact angles for both reservoirs,
443 minimum and maximum conversion factors calculated for Boggy Creek Field (CO₂-
444 dominated) and Katnook Field (methane-dominated) were 0.054 - 0.087 and 0.111 -
445 0.133, respectively.

446

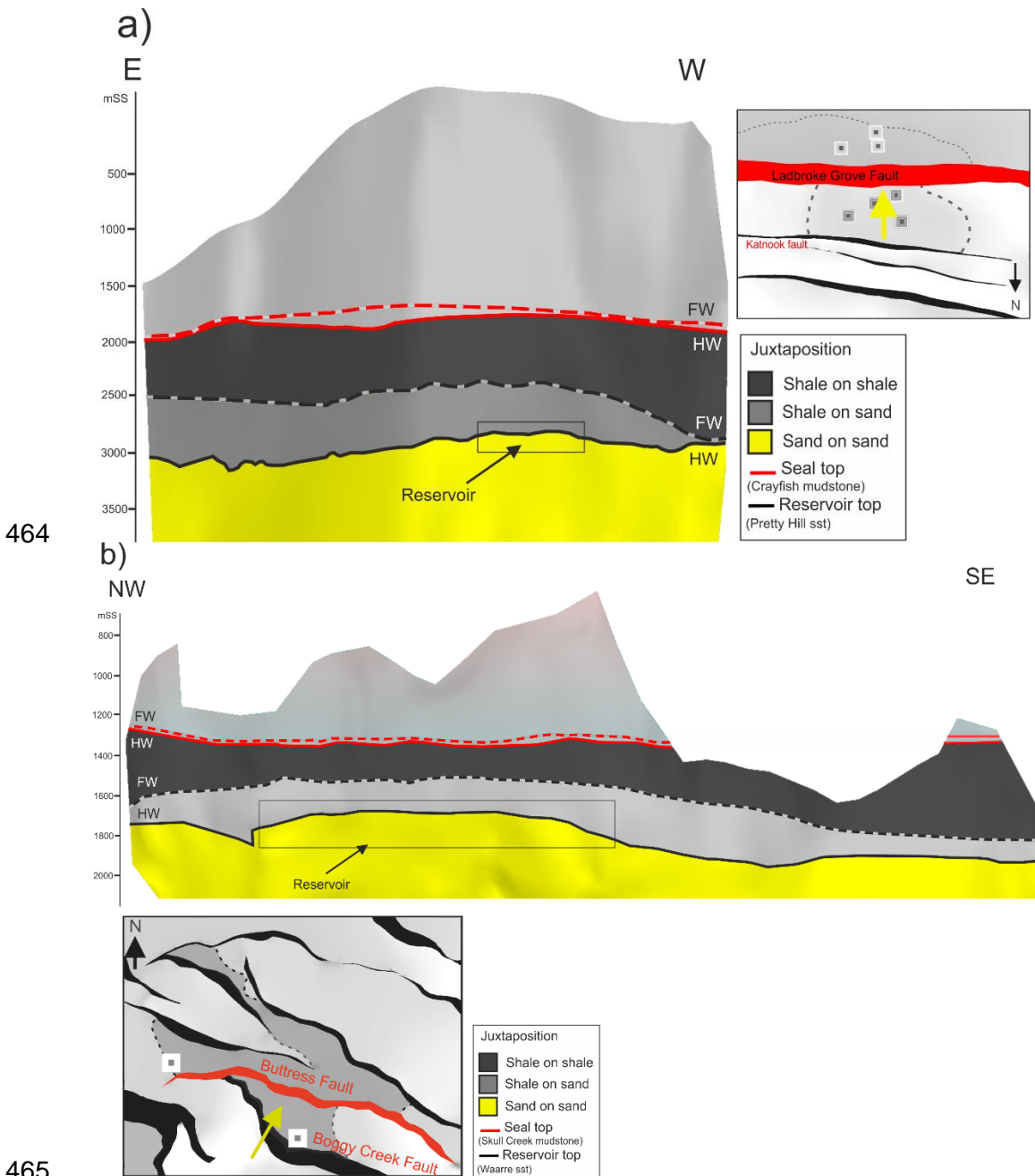
447

5 Results

448

5.1 Structural and fault rock composition results

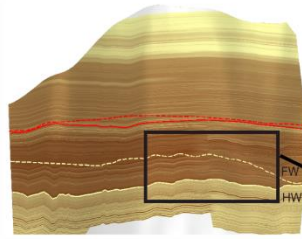
449 The Allan diagrams in Figure 5 show the juxtaposition of lithologies along the strike
450 of the fault planes for Katnook (a) and Boggy Creek (b) reservoirs. The Katnook
451 reservoir is primarily sealed by sand on shale juxtaposition by the Katnook fault to
452 the north, but the field extends to the hanging wall of the Ladbroke Grove fault which
453 is supporting the column to the south (Fig. 5a). The entire extent of the reservoir is
454 juxtaposed against reservoir on the other side of the fault. Similarly, the Boggy
455 Creek field is supported by sand on shale juxtaposition in the footwall of the Boggy
456 Creek fault to the south. The field extends to the hanging wall of the Buttress fault
457 (Fig. 5b), where the reservoir is self-juxtaposed for the entire extent of the gas field.
458 Calculated V-shale values for areas of reservoir self-juxtaposition range between 20
459 and 50% on the Ladbroke Grove Fault and 10% to 80% on the Buttress fault. In the
460 reservoir interval, SGR values range from 35% to 41% on Ladbroke Grove fault and
461 60-70% on the Buttress fault (Fig. 6). SGR values above 20% are considered to be
462 sealing (Yielding et al., 2010), so in both cases the model indicates that the faults
463 are acting as barriers to gas migration.



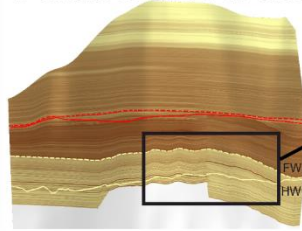
465
 466 *Figure 5. Allan diagrams showing juxtaposition along the strike-view of the faults, viewed*
 467 *from the hanging wall side. Insets show the location of the faults (marked in red), the yellow*
 468 *arrows show the direction of view. a) Ladbroke Grove fault, supporting the southern side of*
 469 *the Katnook gas field (3x vertical exaggeration). b) Buttress fault, supporting the northern*
 470 *side of the Boggy Creek gas field (no vertical exaggeration). Black rectangles show the*
 471 *extent of the gas-bearing reservoir. Horizon intersections on the fault plane are displayed as*
 472 *dashed lines for the footwall side and solid lines for the hanging wall side.*
 473

a) Ladbroke Grove fault, the Katnook gas field

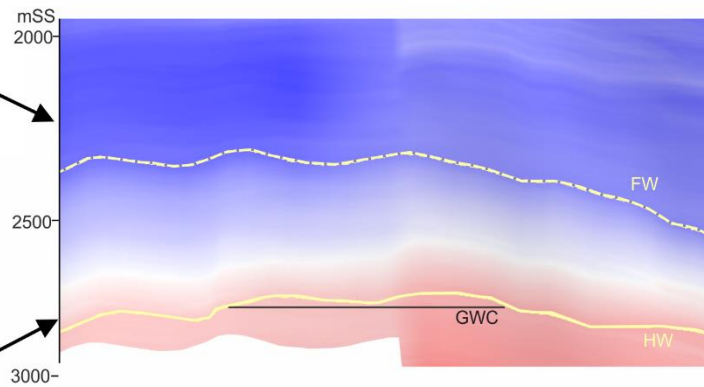
V-Shale on the HW side



V-Shale on the FW side

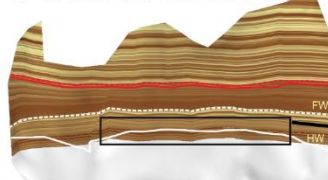


Shale Gouge Ratio

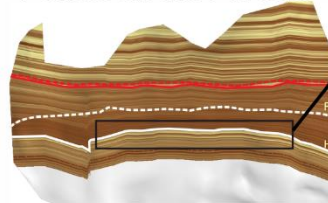


b) Buttress fault, Boggy Creek field

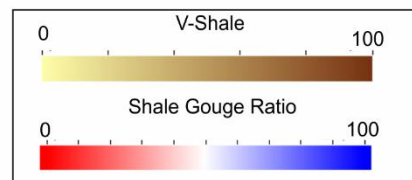
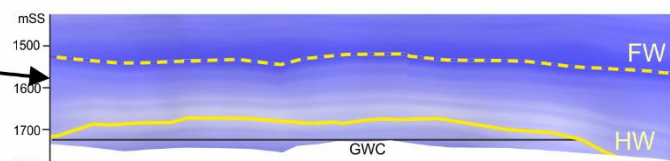
V-Shale on the HW side



V-Shale on the FW side



Shale Gouge Ratio



474

475 *Figure 6. Composite V-Shale curves projected on the HW and FW of the fault plane and the*
476 *calculated SGR values. A) the Ladbroke Grove Fault, SGR range 35-41%. b) The Buttress*
477 *fault, SGR range 60-70%.*

478 5.2 Threshold capillary pressure

479 Across-fault leakage through capillary seal breach commonly occurs where
480 the lowest SGR values coincide with the highest buoyancy pressure on a given fault
481 plane. In the two cases discussed here, the highest points of the trap correlate with
482 the lowest SGR values, making the top of the fault the most likely to leak (Fig. 7).
483 The buoyancy pressure values identified at these points are 0.28 MPa for the
484 Katnook field and 0.29 MPa for the Boggy Creek.

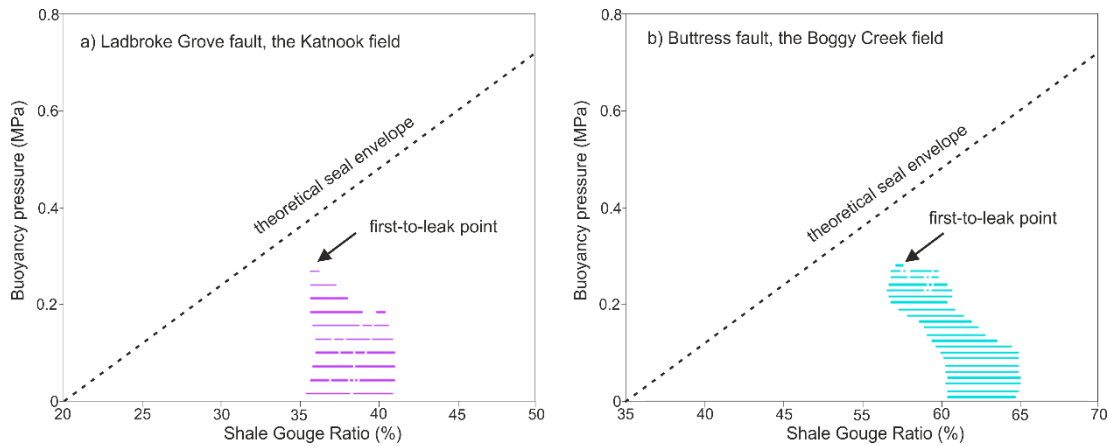
485 The calculated threshold capillary and buoyancy pressures can then be
486 compared at the critical points, where the difference between them represents the
487 amount of extra pressure (or extra gas column) the fault can retain before seal
488 breach. Figure 8 shows the results of the deterministic (a, c) and empirical (b, d)
489 calibrations for the Ladbroke Grove fault in the Katnook field, and the Buttress fault
490 in the Boggy Creek field.

491 The results from both calibrations for the Katnook methane gas field indicate
492 that the current live gas column of 31 metres (equivalent to 0.28 MPa buoyancy
493 pressure) is stable but the fault is close to capillary seal breach. The threshold
494 capillary pressures range from 0.32 to 0.55 MPa, equivalent to a total column of gas
495 between 35 to 57 m according to the deterministic calibration. Empirical calibration
496 suggests the fault seal will be breached at pressures between 0.3 and 0.57 MPa,
497 equivalent to a total gas column of 33 to 63 m. The results from both calibrations are
498 remarkably similar, with the average threshold capillary pressure of 0.42 and 0.43
499 MPa using the deterministic and empirical methods respectively.

500 The deterministic and empirical methods provide different results for the
501 Boggy Creek CO₂ field. The fault is currently supporting a 51 m column of gas,
502 equivalent to a buoyancy pressure of 0.29 MPa. This is close to the upper range
503 values predicted by the deterministic method. The threshold capillary pressure
504 ranges from 0.15 to 0.31 MPa (26 – 55 m of total column height). The predicted
505 average column height is 39 m, slightly under-predicting the sealing potential of the
506 fault. In contrast, the empirical calibration indicates a threshold pressure of 0.65
507 MPa and a maximum column height of 115 m, which is more than double the current
508 amount.

509 The empirical method requires only one parameter of the maximum burial
510 depth. The deterministic method requires three parameters. In the case of the
511 Katnook methane field, the uncertainty in maximum burial depth has the biggest
512 impact on the results and the conversion factor is the second largest uncertainty
513 (see y axis annotation on Fig. 8). In contrast, the uncertainty in the conversion factor
514 has a greater impact on the Boggy Creek CO₂ field results than the maximum burial
515 depth.

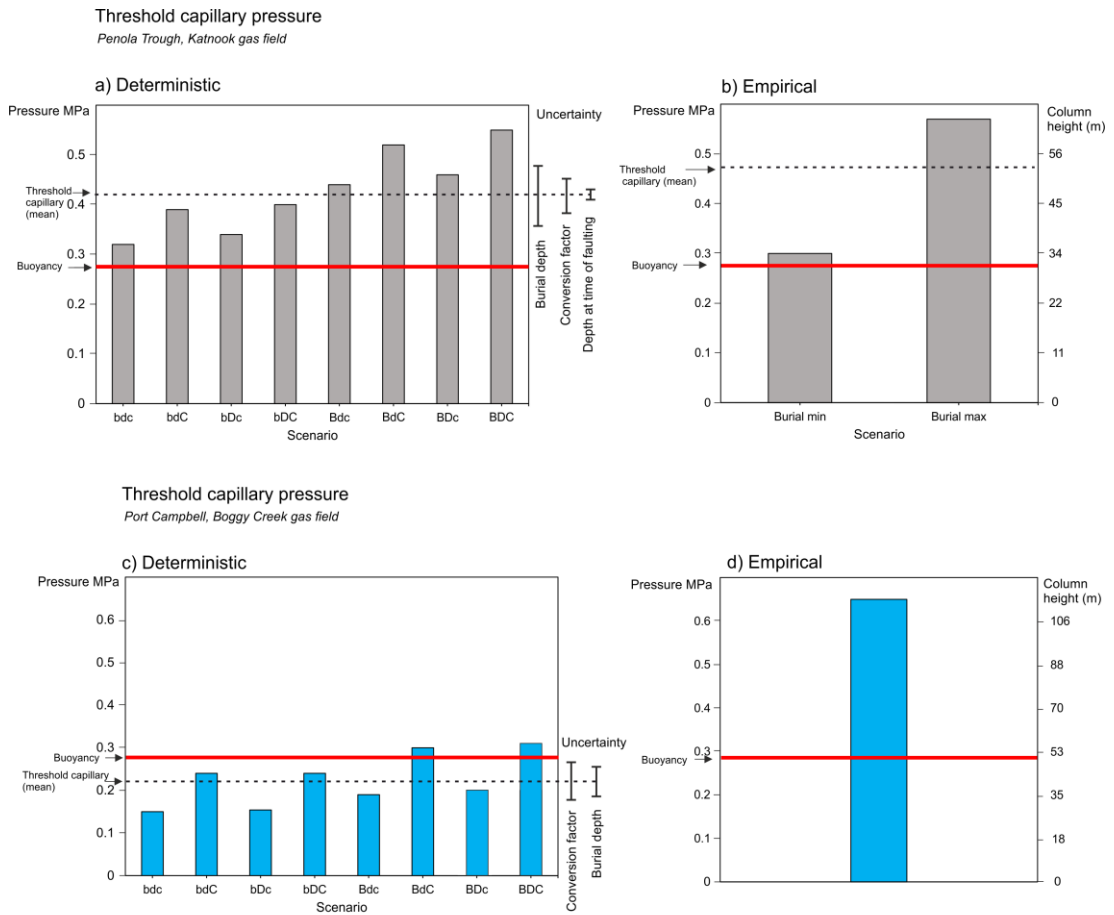
516 The structural spill point at the Katnook field is identified at 2891 m, which
 517 effectively allows a maximum gas column height of 81 m. In Boggy Creek, the
 518 structural spill point occurs at 1956 m, allowing a maximum column height of 272 m.
 519 The maximum column heights identified from the structural perspective of the traps
 520 are all higher than those modelled by fault seal analysis. This means that filling the
 521 traps to the maximum fault-rock threshold pressures derived from all models would
 522 not result in fill-to-spill and therefore both methods indicate that migration to the
 523 adjacent fault trap occurred through the fault rather than through over-spilling.



524

525 *Figure 7. Buoyancy pressure vs SGR calculated for every point of the 3D fault plane within*
 526 *the gas column for a) the Katnook methane field, Penola Trough b) the Boggy Creek CO₂*
 527 *field, Port Campbell. The first-to-leak points in both cases occur where the highest buoyancy*
 528 *pressure coincides with the lowest SGR values (black arrow), which happens to be at the top*
 529 *of the gas fields. Dashed line shows a theoretical seal envelope line. The first-to-leak point is*
 530 *always closest to the seal envelope line.*

531



532
 533 *Figure 8. Bar chart showing threshold capillary pressure results for the Katnook methane*
 534 *field (a, b) and the Boggy Creek CO₂ field (c, d) using deterministic (a, c) and empirical (b, d)*
 535 *SGR calibration algorithms. Conversion to column height displayed on the secondary y axis*
 536 *(same values applicable to both deterministic and empirical method graphs. Red line shows*
 537 *current column height/buoyancy pressure. The Katnook gas column is predicted to be stable*
 538 *by both methods with maximum threshold capillary pressure ranging from 0.32 to 0.55 MPa*
 539 *(deterministic) and 0.3 to 0.57 MPa (empirical). The Boggy Creek field is predicted to be*
 540 *within the upper end of the critical pressure zone by the deterministic method (0.15-0.31*
 541 *MPa) and stable by the empirical method. Labels in deterministic scenarios: B- maximum*
 542 *burial depth, D – depth at the time of faulting, C – conversion factor. Upper and lower case*
 543 *letter indicate maximum and minimum values respectively.*

544

6 Discussion

545

6.1 Addressing the uncertainty in fault seal modelling

546

547

548

549

550

551

552

553

554

555

556

557

The deterministic and empirical methods present a key difference in their definition of the threshold capillary pressure. The deterministic method defines a best fit line through the data points of measured capillary entry pressures during injection experiments to fault rock samples. Therefore, by definition, the method predicts the average threshold pressure for the modelled conditions. In contrast, the fault seal envelopes defining the threshold capillary pressure in the empirical method represent the upper limit of data for buoyancy pressures retained by fault rocks with a given SGR. The threshold pressure returned by the empirical equation is therefore a maximum estimate. In other words, even though the same term of threshold capillary pressure is used by the two methods, the derived value represents somewhat different concepts and presents a different level of uncertainty.

558

559

560

561

562

563

564

565

566

567

568

569

570

571

572

Some uncertainties are inherent to the modelling method and cannot be easily accounted for. The deterministic method is based on threshold capillary pressure measurements of micro-fault samples on the scale of millimetres to centimetres (Sperrevik et al., 2002). The measured clay content of the fault structures is assumed to be represented by SGR when upscaled to use in a predictive way. The method is therefore applied on the assumption that kilometre scale faults behave in the same way as micro structures. In reality this is not strictly the case, with seismic-scale fault zones comprising clay smears, cataclastic zones and multiple planes of deformation (Bense et al., 2016; Faulkner et al., 2010; Fisher and Knipe, 1998; Pei et al., 2015; Shipton and Cowie, 2001), which all add to the total sealing capacity of the fault zone. Detailed fault zone analyses show that the permeability over individual fault zone components can vary considerably (e.g. over 3 orders of magnitude) (Shipton et al., 2002) and therefore upscaling one of those components to be representative of the entire fault zone involves a significant simplification.

573

574

575

The advantage of the empirical method in this respect is that SGR is assumed to be a proxy for the fault sealing properties, which include shale content but also various heterogeneous components of the fault zone. SGR calculated on

576 the 3D surface of the fault planes is the direct input in the calibration as well as in
577 the predictive workflow, which eliminates the uncertainty associated with equating
578 SGR to specific rock properties such as the true volume of shale. The compilation
579 dataset includes data from 7 different basins, covering a wider range of diagenetic
580 conditions relative to the deterministic method which is based on samples from the
581 North Sea (Yielding, 2002).

582 Some of the uncertainties associated with the local geological conditions and
583 fluid properties are parameterised in the deterministic method and therefore can be
584 accounted for. The error bars in Figure 8 a) and c) show the relative uncertainties
585 associated with the different model input parameters. For the two case studies
586 presented here, fluid properties (governing the conversion factor) present a higher
587 uncertainty for CO₂ rather than methane. This is primarily due to the larger IFT
588 range selected for CO₂, but does not suggest that the interfacial tension of CO₂ is
589 less characterised than that of methane. The larger range is due to a relatively
590 higher number of currently available studies, including measurements using different
591 salinity, salt types and gas mixtures, while methane laboratory studies are largely
592 constrained to pure methane and deionized water. In cases where fluid properties
593 are well defined, maximum burial depth is the most significant source of uncertainty,
594 while depth at the time of faulting is the least significant input parameter.

595 6.2 Uncertainty related to fluid properties

596 An important difference between the two methods is the approach to
597 accounting for the fluid properties. The interfacial tension and wettability are
598 parameterised in the deterministic method, making it more versatile, arguably
599 adaptive to CO₂-brine system and more precise in cases where fluid properties are
600 well characterised. The empirical method does not explicitly address the fluid
601 properties, but operates under the assumption that the range of IFT and contact
602 angle configurations in hydrocarbons is small, and that the possible variability of
603 fluid properties is represented in the global dataset compilation. The two important
604 issues with the empirical approach are:

605 a) the uncertainty related to fluid properties is undefined when applied to
606 hydrocarbons.

607 b) the application to CO₂ can only be considered valid in cases where CO₂
608 exhibits properties within the range of those observed in hydrocarbons.

609 These are explained in detail below.

610 6.3 a) Uncertainty related to fluid properties of 611 hydrocarbons in the empirical model

612 To further assess the empirical method application to CO₂, the uncertainty
613 related to the fluid properties of hydrocarbons has to be defined. The percentage
614 error of the capillary threshold pressure (δP_c) from the uncertainty in fluid properties
615 (as standard deviation) can therefore be expressed as, using Equation 1:

$$616 \delta P_c = \frac{\sigma(P_c)}{\mu(P_c)} \times 100\% = \frac{\sigma(2IFT \times \cos\theta)}{\mu(2IFT \times \cos\theta)} \times 100\% \quad (5)$$

617 Where σ is the standard deviation and μ is the average value of the probability
618 distribution. The empirical method uses a data compilation including both oil and
619 methane in reservoirs > 1.5 km depth (Yielding, 2002), and can be assumed to
620 reflect the general IFT and contact angle variability of all hydrocarbons at that depth.
621 The percentage error can therefore be calculated using a random sampling
622 modelling approach with inputs of the probability distribution of IFT and contact
623 angle values in hydrocarbons-brine system. Theoretically, the contact angle is
624 related to the IFT at the interfaces between the solid and the fluids based on the
625 Young's equation, however, the solid-fluid interface presents significant variability
626 based on the type of solid. A significant number of factors affecting the contact angle
627 not directly related to the fluid type exist. We therefore assume the IFT and the
628 contact angle to be independent variables.

629 6.3.1 Defining IFT and wettability range for hydrocarbons

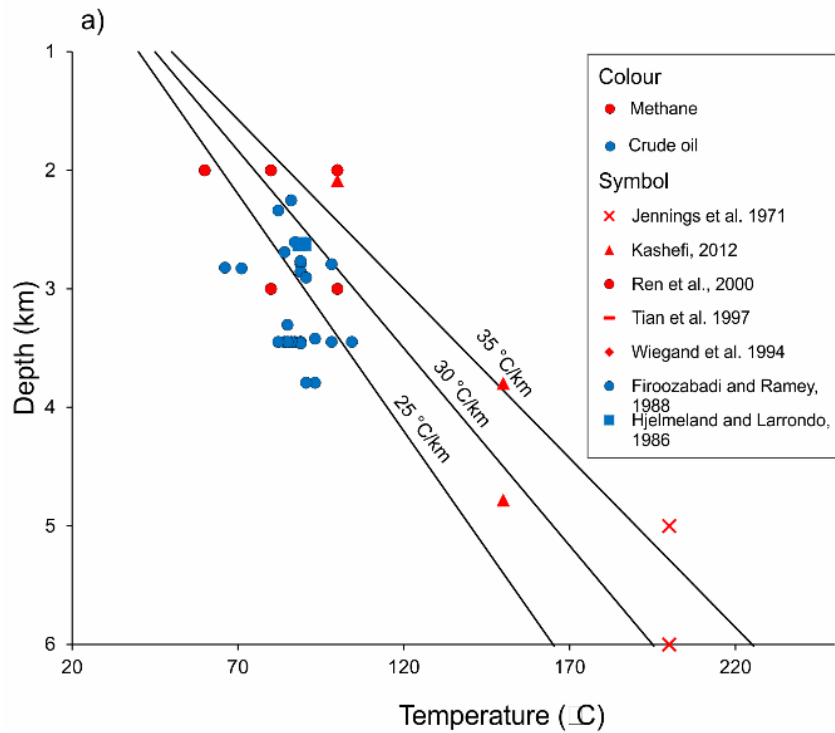
630 The IFT between hydrocarbons and water (or brine) is primarily controlled by
631 the chemical composition of the hydrocarbons, the density contrast between the two
632 phases and temperature (Flock et al., 1986; Hassan et al., 1953; Rajayi and
633 Kantzas, 2011). Pressure mainly affects gas solubility in oil and therefore has a
634 bigger effect on oils with high dissolved gas content (Ghorbani and Mohammadi,
635 2017). Generally, the IFT in hydrocarbons is not well characterised and usually an

636 average IFT of 30-35 mN/m is used for capillary seal modelling purposes (Berg,
637 1975; Robert M. Sneider and Neasham, 1997). Considerable effort has been made
638 to characterise IFT of individual hydrocarbon compounds and derive predictive
639 equations to determine the IFT based on the input of reservoir temperature
640 (Kalantari Meybodi et al., 2016), density difference (Danesh, 1998; Sutton, 2006)
641 and critical fluid temperature (Najafi-Marghmaleki et al., 2016). However, these
642 methods are developed for data compilations of pure aromatics and alkanes, and do
643 not reflect the fluid properties of crude oil at reservoir conditions, which include high
644 percentage of other compounds such as naphthenes and asphaltics (Buckley et al.,
645 1997).

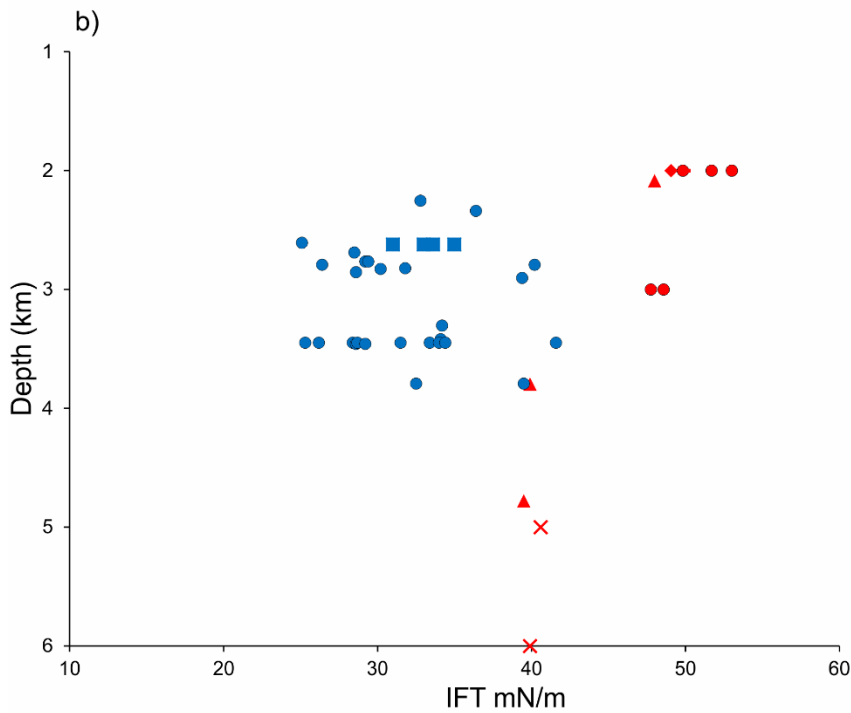
646 There have been relatively few studies presenting IFT measurements in
647 crude oil-water systems, but these can be considered the most reservoir-
648 representative. Figure 9 shows a compilation of laboratory measurements within the
649 envelope of pressures and temperatures valid for geothermal gradients between 25
650 and 35 °C/km and hydrostatic pressure gradient of 10 MPa/km. The compilation
651 includes samples of crude oil above bubble point representing non-degassed oils,
652 below-bubble point oils and methane. The IFT values of crude oil range 26-42 mN/m
653 and are more strongly controlled by chemical differences rather than depth. IFT of
654 methane decreases with depth and ranges from 40 to 53 mN/m. Based on this
655 example dataset, it is assumed that the IFT values of hydrocarbons used in the
656 empirical calibration method are expected to be within a uniform probability
657 distribution with a mean value of 39 ± 8 mN/m (Fig. 10a).

658 In the context of capillary seal modelling, reservoir formations are generally
659 considered to be water-wet in the presence of hydrocarbons (contact angle = 0°)
660 (e.g. Schowalter, 1974; Vavra et al., 1992). This is not strictly true, with mixed-wet
661 and oil-wet states often observed in hydrocarbon reservoirs (Treiber and Owens,
662 1972), often due to mineral surface coating with high polarity crude oil components
663 such as asphaltenes which have high affinity to the reservoir minerals (Alipour
664 Tabrizy et al., 2011; Singh et al., 2016). The degree of oil-wetting is expected to be
665 higher in reservoirs containing high maturity oil and in the presence of carbonate
666 cements, smectite, chlorite, kaolinite and iron-oxides (Barclay and Worden, 2009;
667 Worden and Morad, 2000). Because the contact angle directly affects the calculated
668 column heights and associated threshold capillary pressures, the practice of
669 assuming 0° contact angle in hydrocarbon reservoirs always provides a maximum

670 rather than conservative estimate. In the absence of strong statistical data, we
671 assume that reservoir rocks are more commonly water-wet than oil-wet in the
672 presence of hydrocarbons. This spread of data is best described by an exponential
673 probability distribution ($\beta = 15$), with a mean value of $15 \pm 15^\circ$ (Fig 10b) The lowest
674 values in the range are the most probable. Based on Equation 3, retention of a gas
675 column is only possible when the contact angle is $\leq 90^\circ$ ($\cos\theta > 0$). Because the
676 data set by definition only includes reservoirs with observed columns, contact angles
677 must range between 0 and 90° .



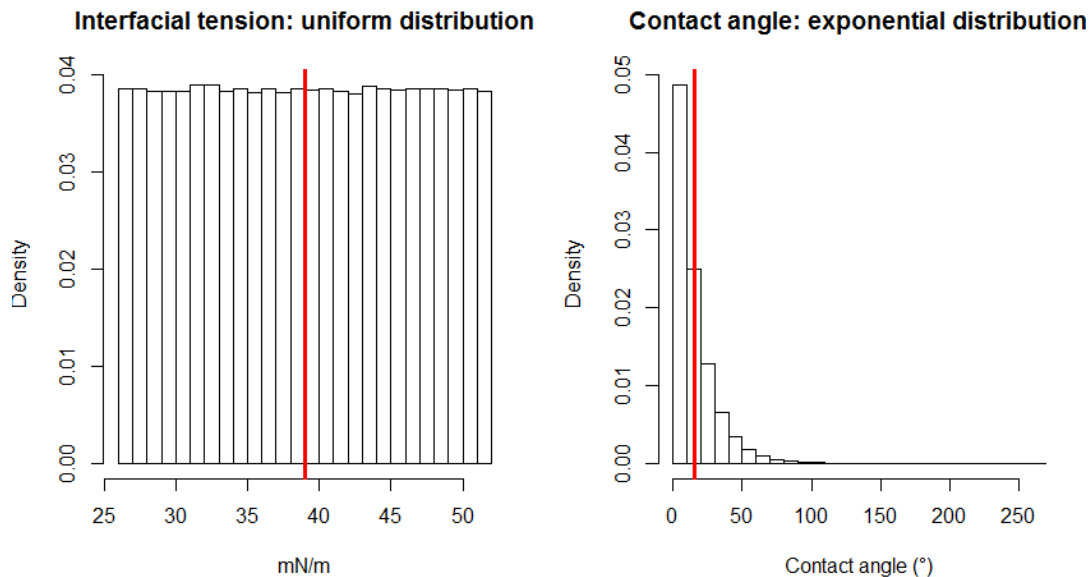
678



679

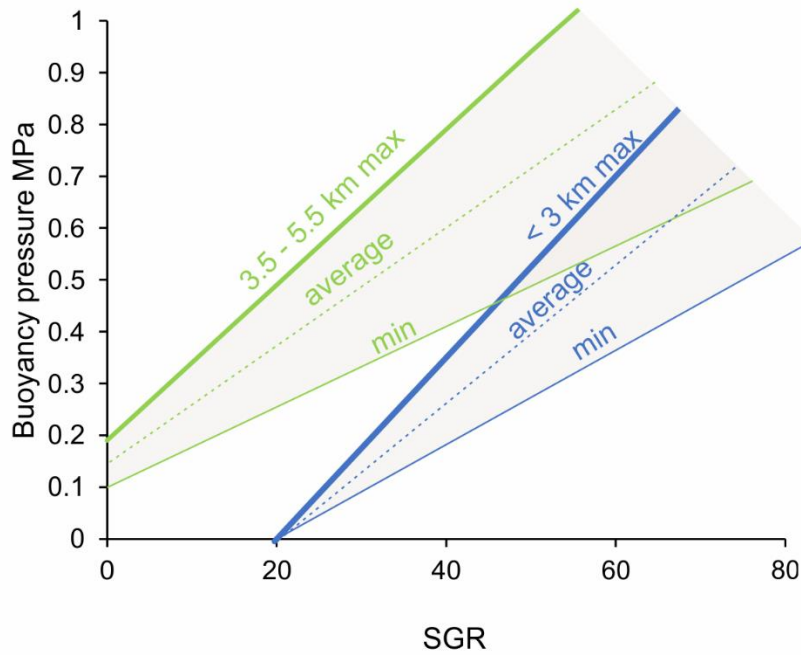
680

681 *Figure 9. IFT of crude oil and methane data compilation from the literature, filtered to*
 682 *conditions applicable to geological pressure and temperature conditions (25 - 35 °C/km*
 683 *geothermal gradient). a) shows the distribution depth vs temperature conditions, b) shows*
 684 *the IFT values of the same data points. Crude oil IFT values range between 26 - 42 mN/m*
 685 *and are uniformly distributed. Methane values range 40 - 53 mN/m and decrease with depth.*
 686 *Combined together, this data represents a uniform distribution.*



687
 688 *Figure 10. Probability distribution of IFT (a) and contact angle (b) in hydrocarbons at*
 689 *reservoir conditions below 2 km depth, defined based on a literature review of laboratory*
 690 *studies (discussed in text). Red vertical line shows mean. IFT is expected to be uniformly*
 691 *distributed with a mean value of 39 ± 8 mN/m. Exponential distribution ($\beta = 15$) best*
 692 *describes the expected contact angle.*
 693

694 Based on the probability distributions of IFT and contact angle determined
 695 above, the percentage error of threshold capillary pressure (δP_c) determined from
 696 Equation 5 using Monte Carlo random sampling analysis ($n = 10^6$) is 24%. Figure 11
 697 shows the seal failure envelopes of the empirical model (Yielding et al., 2010) with
 698 the calculated error added. The seal envelopes define the upper boundary of all
 699 buoyancy pressures observed to be sealed by fault rocks and therefore statistically
 700 represent the higher values within the data distribution or maximum threshold
 701 capillary pressure. We can therefore use the calculated uncertainty to estimate the
 702 average threshold capillary pressure ($P_c - \sigma$) and minimum threshold capillary
 703 pressure ($P_c - 2\sigma$). The uncertainty increases with increasing P_c .



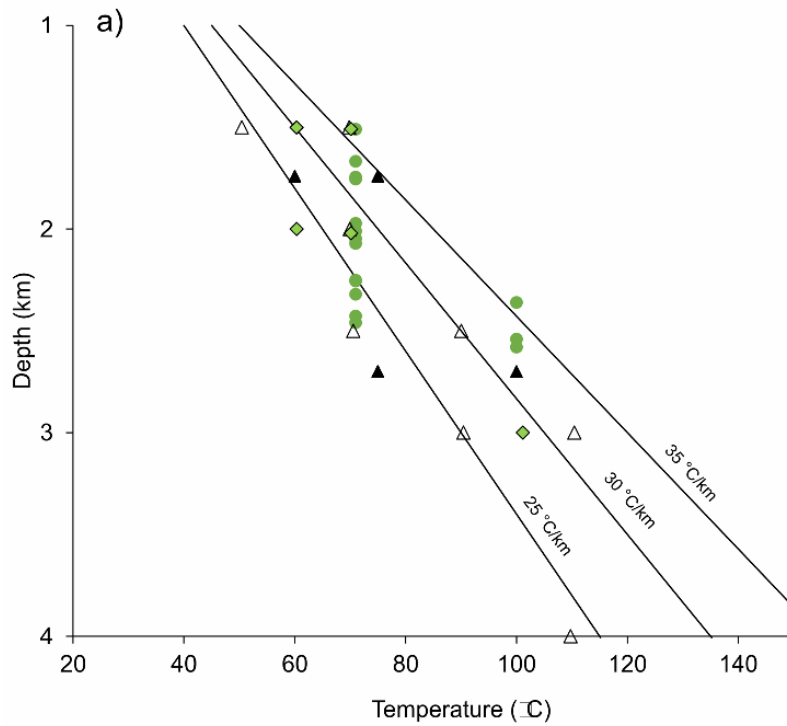
704
 705 *Figure 11. SGR vs Buoyancy pressure with < 3 km and 3.5 - 5.5 km threshold capillary*
 706 *pressure envelopes from Yielding et al. (2010). The thick solid line shows the original*
 707 *maximum threshold capillary pressure. Calculated average (dashed line) and minimum (thin*
 708 *solid line) pressures for given burial depth brackets are also displayed.*
 709

710 *6.3.1.1 Implications for use in hydrocarbons*

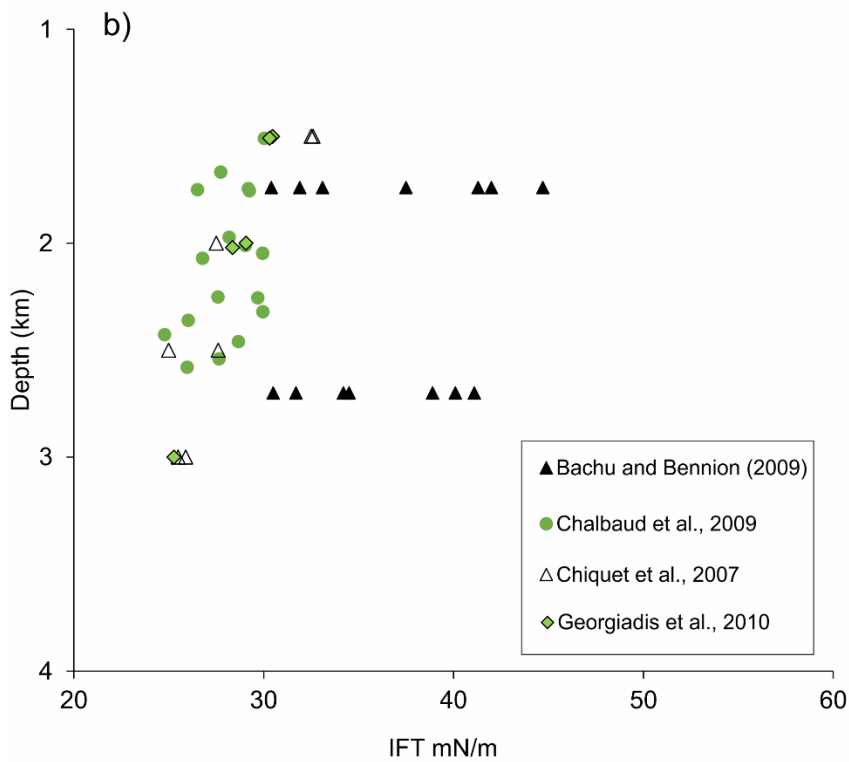
711 The calculated uncertainty envelopes do not change the interpretation of the
 712 empirical calibration method, but rather provide additional constraints that can be
 713 applied in variety of contexts. In cases where capillary pressure modelling is used to
 714 assess the economic viability of the reservoir, the uncertainty can be a useful input
 715 into the risking process. The average threshold capillary pressure value is better
 716 used in the calculation of likely hydrocarbon column heights, bearing in mind that the
 717 true column height can be controlled by many factors independent to fault seal such
 718 as structural spill points and charge. In cases where sufficient geological evidence
 719 exists to indicate that the trap has been filled, the calculated uncertainty envelope
 720 provides means to determine the minimum expected column. The average threshold
 721 capillary pressure value using the empirical method is also more comparable to the
 722 average results of the deterministic method (rather than using the current empirical
 723 max value) when the two are used in conjunction.

724 6.4 b) Empirical method applied to the fluid properties of
725 CO₂

726 In the last decade significant effort has gone into characterising IFT of CO₂
727 at a range of conditions, with existing data covering CO₂/water (Chiquet et al.,
728 2007a; Georgiadis et al., 2010) and CO₂/brine with variable salinity and salt types
729 (Bachu and Bennion, 2009; Chalbaud et al., 2009). IFT has been characterised for
730 mixtures of CO₂ and methane in water (Ren et al., 2000) and brine (Liu et al., 2016).
731 Increasing brine salinity has been shown to increase the IFT in CO₂/brine system
732 with significant deviations in saline and hypersaline conditions (Bachu and Bennion,
733 2009; Chalbaud et al., 2009; Liu et al., 2016). Figure 12 shows results from
734 published laboratory studies filtered to those representative of pressure and
735 temperature conditions in the subsurface (geothermal gradients 25 – 35 °C/km,
736 hydrostatic pressure gradient 10 MPa/km). The data includes pressures above 15
737 MPa (~1.5 km depth), which is in line with depths recommended for safe geological
738 CO₂ sequestration (> 1.2 km) (Miocic et al., 2016). It is apparent that in the
739 supercritical fluid state, depth does not significantly influence the IFT. The most
740 important controlling factor is brine salinity which increases the IFT due to increasing
741 density contrast between CO₂ and the brine. The maximum IFT values of 44.7 and
742 41.1 mN/m at 1.7 km and 2.7 km depth respectively from the study of Bachu and
743 Bennion (2009) are measured in brines of 334 g/L salinity, which is close to the
744 maximum possible salt saturation in water. In comparison, the salinity of UK oil and
745 gas fields ranges from 30 to 227 g/L with an average value of 130 g/L (Gluyas and
746 Hichens, 2003). The IFT range presented here covers the minimum (CO₂-pure
747 water) to maximum (CO₂-hypersaline brine) geologically possible conditions relevant
748 to CO₂ sequestration context (> 1.5 km depth), and also falls within the range
749 observed in liquid hydrocarbons. The IFT values range between 26 to 45 mN/m,
750 which is remarkably similar to IFT range in crude oil (26 – 42 mN/m, Fig. 9).



751



752
753

754 *Figure 12. IFT of CO₂ in water and brine of different salinities, filtered to only display*
 755 *pressure and temperature conditions applicable to geological setting (25-35 °C/km*
 756 *geothermal gradient). a) shows the distribution depth vs temperature conditions, b) shows*
 757 *the IFT values of the same data points. IFT ranges 26-45 mN/m. Datapoints from Bachu and*
 758 *Bennion (2009) show the effects of increasing salinity, with a maximum of 334 g/L resulting*
 759 *in the highest IFT values.*

760 The wettability in CO₂-brine system is a complex issue and cannot be easily
 761 defined as a bracket range for all reservoir conditions. The conditions of many
 762 experimental set ups are very different to reservoir conditions, as discussed in
 763 section 4.1.4, therefore the upscaling of single mineral experimental results to
 764 reservoir is problematic. Irrespective of this variation, the most significant
 765 observation emerging from CO₂-brine lab studies is the change in wettability caused
 766 by pressure. This is observed when CO₂ changes from gaseous to supercritical fluid
 767 phase at around 8 MPa. It is presently not understood if the change in wettability is
 768 related to the process of phase change or to the physical properties of supercritical
 769 CO₂. Single mineral studies reveal that contact angles are significantly higher in the
 770 presence of physosilicate minerals relative to quartz; this effect increases with
 771 pressure and temperature (Arif et al., 2016). This could mean that increasing clay
 772 fraction in the fault rock which correlates with increasing SGR, may also have an
 773 opposing negative effect to the overall sealing potential of the rock. The important
 774 step in reducing the current uncertainty and the spread of data between different
 775 studies is to move to whole-rock rather than single-mineral studies. The
 776 understanding of the uncertainty related to CO₂ fluid properties would be greatly
 777 enhanced by availability of more comprehensive IFT and CA studies, at reservoir
 778 pressure and temperature conditions using core flooding experiments and
 779 employing X-ray microtomography techniques (e.g. Andrew et al., 2014).

780 In summary, the IFT values for CO₂ are similar to those of oil, while methane
 781 IFT values are higher on average. The contact angles in CO₂-brine system present
 782 a higher level of uncertainty and are hard to evaluate as a generic range. IFT and
 783 contact angles can however be defined with higher confidence for specific reservoir
 784 conditions, as exemplified by this study.

785 6.4.1 Conversion factor from hydrocarbons to CO₂

786 This work has defined an average value (μ) of the probability distributions of
 787 IFT (39 mN/m) and CA (15°) for hydrocarbons under pressure and temperature
 788 conditions included in the calibration dataset by Yielding et al. (2010). This means
 789 that the calculated threshold capillary pressure of hydrocarbons can be converted to
 790 CO₂-brine system for chosen IFT and CA values of CO₂:

$$791 \quad P_c(CO_2) = P_c \times \frac{IFT_{CO_2} \times \cos\theta_{CO_2}}{\mu IFT_h \times \mu \cos\theta_h} \quad (6)$$

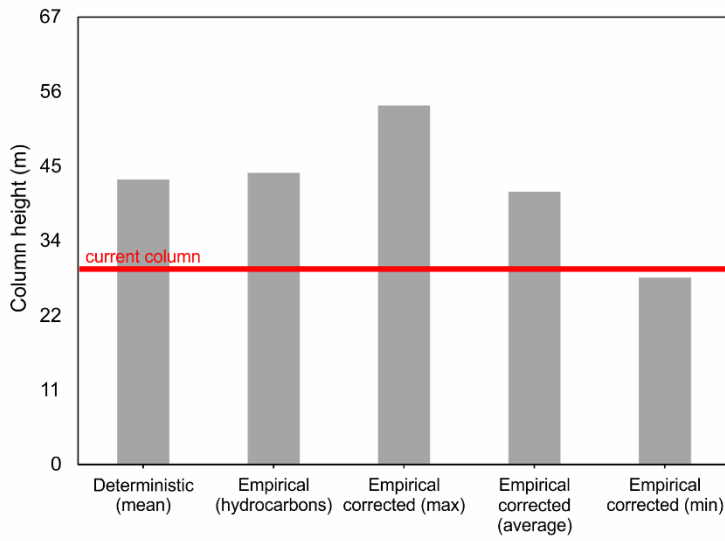
792 This can also be applicable to hydrocarbons in instances where IFT and CA
793 are well defined and significantly different to the average values.

794 Figure 13 shows calculated column heights calculated using the standard
795 empirical and deterministic methods, compared to the empirical model after
796 conversion to CO₂ using Equation 6 (maximum value) and calculated average and
797 minimum values. For the Katnook methane system, the correction factor increases
798 the column heights for methane due to higher IFT, but the overall change is not
799 significantly different from the original empirical model. The current column is
800 predicted to be stable regardless of the correction.

801 The maximum column height for the Boggy Creek CO₂ field is reduced by
802 the correction, with the average empirical value slightly higher than the column
803 height value known to be held by the fault. This prediction is in closer agreement to
804 the deterministic model, and is more likely to be correct based on the geochemistry
805 of the fields, indicating higher mantle CO₂ contents at Boggy Creek than in the
806 adjacent Buttress field and suggesting initial charge to Boggy Creek lead to
807 subsequent migration into Buttress. The current column in Boggy Creek is not near
808 the structural spill point, suggesting the CO₂ transfer between the fields occurred
809 through the fault rock, and the current column is therefore expected to be near the
810 threshold value.

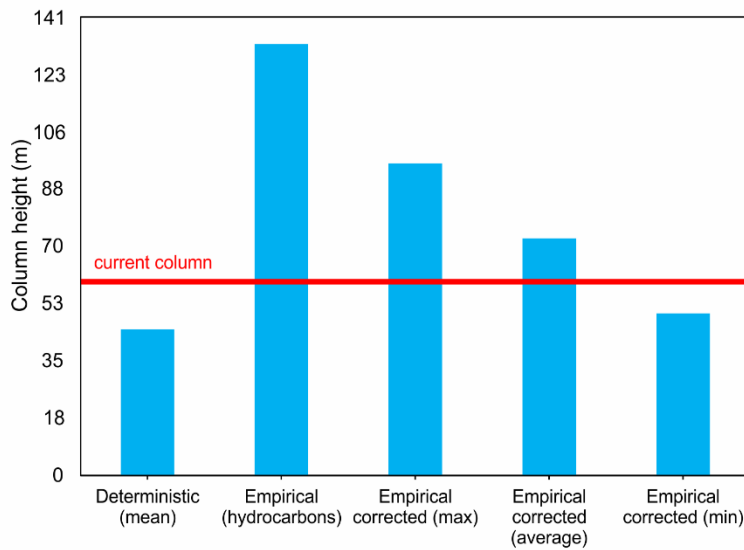
Gas column heights (m)

a) Penola Trough, Katnook gas field (methane)



811

b) Port Campbell, Boggy Creek gas field (CO₂)



812

813

814

815

816

Figure 13. Gas column heights a) Penola Trough, Katnook field b) Port Campbell, Boggy Creek field. Current live columns marked in red. Models shown: deterministic (Sperrevik et al., 2002), empirical (Yielding et al., 2010), empirical corrected max, average and min values (this work).

7 Conclusions

818 Two gas fields sealed by fault rocks were examined to compare the standard
819 fault seal analysis techniques applied to methane-brine and CO₂-brine systems. In
820 both cases, the column heights supported by the fault rocks were known, and
821 geochemical gas analysis provided evidence for across-fault connectivity. This
822 allowed us to assess and compare the strengths and weaknesses of two fault seal
823 calibration methods (Sperrevik et al., 2002; Yielding et al., 2010).

824 The deterministic method predicted critical buoyancy pressure in Katnook
825 (methane) and Boggy Creek (CO₂) fields. The empirical method predicted critical
826 buoyancy pressure in Katnook field and well below threshold pressure in the Boggy
827 Creek field. However, after accounting for uncertainty and applying the newly
828 proposed correction for CO₂, the method also predicted criticality. Thus, the
829 geochemistry and fault seal analysis results corroborate each other.

830 CO₂ fluid properties and their differences from hydrocarbons have been
831 previously identified as the biggest uncertainty associated with fault seal application
832 to CO₂ systems. However, an extensive literature review showed that a similar
833 spread in IFT values exists within the hydrocarbons, due to the wide range of
834 possible chemical compositions of crude oil. This means that IFT in CO₂-brine
835 system is easier to identify for particular pressure and temperature conditions than
836 in liquid hydrocarbons. Wettability of hydrocarbons is not very well characterised
837 either, and the recent academic focus to CO₂ sequestration applications means that
838 currently far more laboratory experimental data exists for CO₂-brine systems.
839 Perhaps surprisingly, the main challenge in adapting fault seal modelling techniques
840 from hydrocarbons to CO₂ is the uncertainty associated to the hydrocarbon
841 properties.

842 The two fault seal prediction methods discussed here come with different
843 inherent uncertainties and are best used in conjunction, bearing in mind the
844 differences in the approach. The deterministic method (Sperrevik et al., 2002) can
845 be applied to different fluids via the input of IFT and CA. This work has presented a
846 similar conversion factor system applied to the empirical method (Bretan et al.,
847 2003; Yielding et al., 2010). To do this, an average range of IFT and CA in
848 hydrocarbons under reservoir conditions was determined from literature review. The

849 uncertainty related to the spread in fluid properties was calculated to be 24% of the
850 calculated threshold capillary pressure value. This finding does not change the
851 application of the empirical method, which by definition provides a maximum
852 estimate for capillary threshold pressures. However, it allows to constrain an
853 average and minimum capillary pressure values, which can be used to ascertain
854 'most likely' and minimum column heights in hydrocarbon exploration. The newly
855 defined average capillary threshold pressure value also allows for better comparison
856 with the deterministic method, which by definition models average rather than
857 maximum pressures.

858 In application to CO₂ storage, where a full column is fully or partially sealed
859 by a fault, the buoyancy pressure must not exceed the minimum threshold capillary
860 pressure value. However, the minimum values discussed here do not equate to safe
861 or recommended buoyancy pressures for CCS contexts. Future studies should
862 define the recommended limit in relation to the minimum threshold capillary pressure
863 values defined here, based on risk analysis and regulatory guidelines.

864 The case study of the Boggy Creek CO₂ field demonstrates that IFT can be
865 very well constrained for particular target reservoir conditions. The definition of CA
866 remains more problematic, because in addition to the dependency on reservoir
867 conditions and brine composition, the CA also depends on the chemical and textural
868 properties of the fault/reservoir rock minerals. This presents two main issues, firstly,
869 that the mineralogy and other properties such as pore-space surface roughness of a
870 particular target reservoir has to be known in detail. This should be easily overcome
871 in the CCS context, where reservoir core studies will be undertaken before the final
872 site selection. Secondly, accurate measurements of CA for the range of possible
873 conditions. Recent whole-rock microtomography-based studies have started
874 providing data from experimental set ups that closely reflect real reservoir conditions
875 (Andrew et al., 2014, Garing et al., 2019). Future studies should expand these
876 experiments to fault and phyllosilicate-rich rocks. As more data on fluid properties of
877 hydrocarbons and CO₂ becomes available, the uncertainty related to conversion
878 between the two systems will decrease.

879 8 Acknowledgments

880 This work was supported by an EPSRC PhD studentship in partnership with
881 CO2CRC and Badley Geoscience Ltd. Badley Geoscience are also thanked for the
882 use of the TrapTester software. We thank Peter Boulton and Paul Lyon for providing
883 3D models of Penola Trough and Jennifer Ziesch for sharing the 3D model of Port
884 Campbell and CO2CRC for providing the seismic data. Thanks to Eric Tenthorey for
885 guidance and help with accessing the data. Gareth Johnson was supported by
886 EPSRC Grant EP/P026214/1 and the Faculty of Engineering at the University of
887 Strathclyde.

888 9 References

889 Alipour Tabrizy, V., Denoyel, R., Hamouda, A.A., 2011. Characterization of
890 wettability alteration of calcite, quartz and kaolinite: Surface energy analysis.
891 Colloids Surfaces A Physicochem. Eng. Asp. 384, 98–108.
892 <https://doi.org/10.1016/j.colsurfa.2011.03.021>

893 Allan, U.S., 1989. Model for hydrocarbon migration and entrapment within
894 faulted structures. Am. Assoc. Pet. Geol. Bull. 73, 803–811.

895 Andrew, M., Bijeljic, B., Blunt, M.J., 2014. Pore-scale contact angle
896 measurements at reservoir conditions using X-ray microtomography. Adv. Water
897 Resour. 68, 24–31. <https://doi.org/10.1016/J.ADVWATRES.2014.02.014>

898 Arif, M., Al-yaseri, A.Z., Barifcani, A., Lebedev, M., Iglauer, S., 2016. Journal
899 of Colloid and Interface Science Impact of pressure and temperature on CO₂ –
900 brine – mica contact angles and CO₂ – brine interfacial tension : Implications for
901 carbon geo-sequestration 462, 208–215. <https://doi.org/10.1016/j.jcis.2015.09.076>

902 Asquith, G.B., Krygowski, D., Gibson, C.R., 2004. Basic well log analysis.
903 American Association of Petroleum Geologists Tulsa.

904 Bachu, S., Bennion, D.B., 2009. Interfacial tension between CO₂,
905 freshwater, and brine in the range of pressure from (2 to 27) MPa, temperature from
906 (20 to 125) °C, and water salinity from (0 to 334 000) mg L⁻¹. J. Chem. Eng. Data
907 54, 765–775. <https://doi.org/10.1021/jc800529x>

908 Barclay, S.A., Worden, R.H., 2009. Effects of reservoir wettability on quartz
909 cementation in oil fields. *Quartz Cem. sandstones* (Eds RH Worden S. Morad).
910 Spec. Publication 29, 103–117.

911 Bense, V.F., Shipton, Z.K., Kremer, Y., Kampman, N., 2016. Fault zone
912 hydrogeology: introduction to the special issue. *Geofluids* 16, 655–657.
913 <https://doi.org/10.1111/gfl.12205>

914 Berg, R.R., 1975. *Capillary Pressures in Stratigraphic Traps*.

915 Bikkina, P.K., 2011. Contact angle measurements of CO₂–water–
916 quartz/calcite systems in the perspective of carbon sequestration. *Int. J. Greenh.*
917 *Gas Control* 5, 1259–1271. <https://doi.org/10.1016/J.IJGGC.2011.07.001>

918 Boreham, C.J., Hope, J.M., Jackson, P., Davenport, R., Earl, K.L., Edwards,
919 D.S., Logan, G.A., Krassay, A.A., 2004. Gas – oil – source correlations in the Otway
920 Basin, southern Australia. *Petroleum Exploration Society of Australia (PESA)*, pp.
921 19–22.

922 Boult, P., Lyon, P., Camac, B., Hunt, S., Zwingmann, H., 2008. Unravelling
923 the complex structural history of the Penola Trough – revealing the St George Fault.
924 PESA East. Australas. Basins Symp. III 14–17.

925 Boult, P.J., Hibbert, J.E., 2002. *The petroleum geology of South Australia.*
926 Vol. 1: Otway Basin. 2nd edn. South Australia. Department of Primary Industries
927 and Resources. *Petroleum Geology of South Australia Series, Vol. 1.*

928 Boult, P.J., Johns, D.R., Lang, S.C., 2004. Subsurface plumbing of the
929 Crayfish Group in the Penola Trough: Otway Basin, in: *Eastern Australasian Basins*
930 Symposium II. *Petroleum Exploration Society of Australia (PESA)*, pp. 483–498.

931 Bretan, P., Yielding, G., Jones, H., 2003. Using calibrated shale gouge ratio
932 to estimate hydrocarbon column heights. *Am. Assoc. Pet. Geol. Bull.* 87, 397–413.
933 <https://doi.org/10.1306/08010201128>

934 Bretan, P., Yielding, G., Mathiassen, O.M., Thorsnes, T., 2011. Fault-seal
935 analysis for CO₂ storage: an example from the Troll area, Norwegian Continental
936 Shelf. *Pet. Geosci.* 17, 181–192. <https://doi.org/10.1144/1354-079310-025>

937 Briguglio, D., Hall, M., Keetley, J., 2015. Structural evolution of the Early
938 Cretaceous depocentres, Otway Basin, Victoria. *Aust. J. Earth Sci.* 1–17.
939 <https://doi.org/10.1080/08120099.2015.1084048>

940 Buckley, J.S., Liu, Y., Xie, X., Morrow, N.R., 1997. Asphaltenes and crude oil
941 wetting-the effect of oil composition. *SPE J.* 2, 107–119.

942 Chalbaud, C., Robin, M., Lombard, J.-M., Martin, F., Egermann, P., Bertin,
943 H., 2009. Interfacial tension measurements and wettability evaluation for geological
944 CO₂ storage. *Adv. Water Resour.* 32, 98–109.
945 <https://doi.org/10.1016/J.ADVWATRES.2008.10.012>

946 Chiquet, P., Daridon, J.-L., Broseta, D., Thibeau, S., 2007a. CO₂/water
947 interfacial tensions under pressure and temperature conditions of CO₂ geological
948 storage. *Energy Convers. Manag.* 48, 736–744.
949 <https://doi.org/10.1016/j.enconman.2006.09.011>

950 Chiquet, P., Daridon, J.L., Broseta, D., Thibeau, S., 2007b. CO₂/water
951 interfacial tensions under pressure and temperature conditions of CO₂ geological
952 storage. *Energy Convers. Manag.* 48, 736–744.
953 <https://doi.org/10.1016/j.enconman.2006.09.011>

954 Chivas, A.R., Barnes, I., Evans, W.C., Lupton, J.E., Stone, J.O., 1987. Liquid
955 carbon dioxide of magmatic origin and its role in volcanic eruptions. *Nature* 326,
956 587–589. <https://doi.org/10.1038/326587a0>

957 Cockshell, C.D., O'Brien, G.W., McGee, A., Lovibond, R., Perincek, D.,
958 Higgins, R., 1995. Western Otway Crayfish Group troughs. *APPEA J.* 35, 385–404.

959 Dance, T., 2013. Assessment and geological characterisation of the
960 CO₂CRC Otway Project CO₂ storage demonstration site: From prefeasibility to
961 injection. *Mar. Pet. Geol.* 46, 251–269.
962 <https://doi.org/10.1016/j.marpetgeo.2013.06.008>

963 Danesh, A., 1998. PVT and phase behaviour of petroleum reservoir fluids.
964 Elsevier.

965 Daniel, R.F., Kaldi, J.G., 2009. Evaluating Seal Capacity of Cap Rocks and
966 Intraformational Barriers for CO₂ Containment 335–345.
967 <https://doi.org/10.1306/13171247St59227>

968 Duddy, I.R., 1997. Focussing exploration in the Otway Basin: understanding
969 timing of source rock maturation. *APPEA J.* 37, 178–191.

970 Espinoza, D.N., Santamarina, J.C., 2010. Water-CO₂ -mineral systems:
971 Interfacial tension, contact angle, and diffusion-Implications to CO₂ geological
972 storage. *Water Resour. Res.* 46. <https://doi.org/10.1029/2009WR008634>

973 Jennings, H.Y., Newman, G.H., 1971. The effect of temperature and
974 pressure on the interfacial tension of water against methane-normal decane
975 mixtures. *Soc. Pet. Eng. J.* 11, 171–175.

976 Farokhpour, R., Bjørkvik, B.J.A., Lindeberg, E., Torsæter, O., 2013. CO₂
977 Wettability Behavior During CO₂ Sequestration in Saline Aquifer -An Experimental
978 Study on Minerals Representing Sandstone and Carbonate. *Energy Procedia* 37,
979 5339–5351. <https://doi.org/10.1016/J.EGYPRO.2013.06.452>

980 Faulkner, D.R., Jackson, C.A.L., Lunn, R.J., Schlische, R.W., Shipton, Z.K.,
981 Wibberley, C.A.J., Withjack, M.O., 2010. A review of recent developments
982 concerning the structure, mechanics and fluid flow properties of fault zones. *J.*
983 *Struct. Geol.* 32, 1557–1575.

984 Firoozabadi, A., Ramey, H.J., Ramey Jr, H.J., 1988. Surface tension of
985 water-hydrocarbon systems at reservoir conditions. *J. Can. Pet. Technol.* 27.

986 Fisher, Q.J., Knipe, R.J., 1998. Fault sealing processes in siliciclastic
987 sediments. *Geol. Soc. London, Spec. Publ.* 147, 117–134.
988 <https://doi.org/10.1144/GSL.SP.1998.147.01.08>

989 Flock, D.L., Le, T.H., Gibeau, J.P., 1986. The effect of temperature on the
990 interfacial tension of heavy crude oils using the pendent drop apparatus. *J. Can.*
991 *Pet. Technol.* 3.

992 Garing, C., Benson, S.M., 2019. CO₂ Wettability of Sandstones: Addressing
993 Conflicting Capillary Behaviors. *Geophys. Res. Lett.* 46, 776–782.
994 <https://doi.org/10.1029/2018GL081359>

995 Georgiadis, A., Maitland, G., Trusler, J.P.M., Bismarck, A., 2010. Interfacial
996 tension measurements of the (H₂O + CO₂) system at elevated pressures and
997 temperatures. *J. Chem. Eng. Data* 55, 4168–4175.
998 <https://doi.org/10.1021/je100198g>

999 Ghorbani, M., Mohammadi, A.H., 2017. Effects of temperature, pressure and
1000 fluid composition on hydrocarbon gas - oil interfacial tension (IFT): An experimental
1001 study using ADSA image analysis of pendant drop test method. *J. Mol. Liq.* 227,
1002 318–323. <https://doi.org/10.1016/J.MOLLIQ.2016.11.110>

1003 Gibson, R.G., 1998. Physical character and fluid-flow properties of
1004 sandstone-derived fault zones. *Geol. Soc. London, Spec. Publ.* 127, 83–97.

1005 Gluyas, J.G., Hitchens, H.M., 2003. United Kingdom oil and gas fields:
1006 commemorative millennium volume.

1007 Guariguata-Rojas, G.J., Underhill, J.R., 2017. Heriot-Watt University
1008 Implications of Early Cenozoic uplift and fault reactivation for carbon storage in the
1009 Moray Firth Basin Implications of Early Cenozoic uplift and fault reactivation for
1010 carbon storage in the Moray Firth Basin. <https://doi.org/10.1190/int-2017-0009.1>

1011 Hassan, M.E., Nielsen, R.F., Calhoun, J.C., 1953. Effect of Pressure and
1012 Temperature on Oil-Water Interfacial Tensions for a Series of Hydrocarbons. *J. Pet.*
1013 *Technol.* 5, 299–306. <https://doi.org/10.2118/298-G>

1014 Higgs, K.E., Haese, R.R., Golding, S.D., Schacht, U., Watson, M.N., 2015.
1015 The Pretty Hill Formation as a natural analogue for CO₂ storage: An investigation of
1016 mineralogical and isotopic changes associated with sandstones exposed to low,
1017 intermediate and high CO₂ concentrations over geological time. *Chem. Geol.* 399,
1018 36–64. <https://doi.org/10.1016/j.chemgeo.2014.10.019>

1019 Hjelmeland, O.S., Larrondo, L.E., 1986. Experimental Investigation of the
1020 Effects of Temperature, Pressure, and Crude Oil Composition on Interfacial
1021 Properties. *SPE Reserv. Eng.* 1, 321–328. <https://doi.org/10.2118/12124-PA>

1022 Hough, E.W., Rzasa, M.J., Wood, B.B., Oil, S., Co, G., 1951. Interfacial
1023 Tensions at Reservoir Pressures and Temperatures ; Apparatus and the Water-
1024 Methane System. J. Pet. Trans. AIME 192, 57–60. <https://doi.org/10.2118/951057-G>

1025 Iglauer, S., 2018. Optimum storage depths for structural CO₂ trapping. Int. J.
1026 Greenh. Gas Control 77, 82–87. <https://doi.org/10.1016/J.IJGGC.2018.07.009>

1027 Iglauer, S., Pentland, C.H., Busch, A., 2015. CO₂ wettability of seal and
1028 reservoir rocks and the implications for carbon geo-sequestration. Water Resour.
1029 Res. 51, 729–774. <https://doi.org/10.1002/2014WR015553>

1030 Jung, J.-W., Wan, J., 2012. Supercritical CO₂ and Ionic Strength Effects on
1031 Wettability of Silica Surfaces: Equilibrium Contact Angle Measurements. Energy &
1032 Fuels 26, 6053–6059. <https://doi.org/10.1021/ef300913t>

1033 Kalantari Meybodi, M., Daryasafar, A., Karimi, M., 2016. Determination of
1034 hydrocarbon-water interfacial tension using a new empirical correlation. Fluid Phase
1035 Equilib. 415, 42–50. <https://doi.org/10.1016/J.FLUID.2016.01.037>

1036 Karolytè, R., 2018. The migration and retention of CO₂ and methane in the
1037 Otway Basin and south-east Australia: an integrated geochemical and structural
1038 analysis. University of Edinburgh.

1039 Karolytè, R., Johnson, G., Györe, D., Serno, S., Flude, S., Stuart, F.M.,
1040 Chivas, A.R., Boyce, A., Gilfillan, S.M.V., 2019. Tracing the migration of mantle CO₂
1041 in gas fields and mineral water springs in south-east Australia using noble gas and
1042 stable isotopes. Geochim. Cosmochim. Acta 259, 109–128.

1043 Kashefi, K., 2012. Measurement and modelling of interfacial tension and
1044 viscosity of reservoir fluids. Thesis. Heriot-Watt University.

1045 Knipe, R.J., 1997. Juxtaposition and seal diagrams to help analyze fault
1046 seals in hydrocarbon reservoirs. Am. Assoc. Pet. Geol. Bull. 81, 187–195.

1047 Lehner, F.K., Pilaar, W.F., 1997. The emplacement of clay smears in
1048 synsedimentary normal faults: inferences from field observations near Frechen,
1049 Germany, in: Norwegian Petroleum Society Special Publications. Elsevier, pp. 39–
1050 50.

1051 Lindsay, N.G., Murphy, F.C., Walsh, J.J., Watterson, J., Flint, S., Bryant, I.D.,
1052 1993. Outcrop studies of shale smears on fault surfaces. *Geol. Model. Hydrocarb.*
1053 *Reserv. outcrop Analog.* 15, 113–123.

1054 Lisk, M., 2004. Constraints on the oil prospectivity of the Penola Trough,
1055 onshore Otway Basin.

1056 Little, B.M., Phillips, S.E., 1995. Detrital and authigenic mineralogy of the
1057 Pretty Hill Formation in the Penola Trough, Otway Basin: implications for future
1058 exploration and production. *APPEA J.* 35, 538–557.

1059 Liu, Y., Li, H.A., Okuno, R., 2016. Measurements and Modeling of Interfacial
1060 Tension for CO₂/CH₄/Brine Systems under Reservoir Conditions. *Ind. Eng. Chem.*
1061 *Res.* 55, 12358–12375. <https://doi.org/10.1021/acs.iecr.6b02446>

1062 Lovibond, R., Suttill, R.J., Skinner, J.E., Aburas, A.N., 1995. The
1063 hydrocarbon potential of the Penola Trough, Otway Basin. *APPEA J.* 35, 358–371.

1064 Lyon, Boulton, P.J., Hillis, R.R., Mildren, S.D., 2005. Sealing by Shale Gouge
1065 and Subsequent Seal Breach by Reactivation: A Case Study of the Zema Prospect,
1066 Otway Basin. *Eval. fault cap rock seals AAPG Hedb. Ser. no. 2* 179–197.
1067 <https://doi.org/10.1306/1060764H23169>

1068 Lyon, P.J., Boulton, P.J., Hillis, R.R., Bierbrauer, K., 2007. Basement controls
1069 on fault development in the Penola Trough, Otway Basin, and implications for fault-
1070 bounded hydrocarbon traps. *Aust. J. Earth Sci.* 54, 675–689.
1071 <https://doi.org/10.1080/08120090701305228>

1072 Lyon, P.J., Boulton, P.J., Mitchell, a, Hillis, R.R., 2004. Improving fault
1073 geometry interpretation through ‘ pseudo-depth ’ conversion of seismic data in the
1074 Penola Trough , Otway Basin . 19–22.

1075 Lyon, P.J., Boulton, P.J., Watson, M.N., Hillis, R., 2005. A systematic fault seal
1076 evaluation of the Ladbroke Grove and Pyrus traps of the Penold Trough, Otway
1077 Basin. *Aust. Pet. Prod. Explor. Assoc. J.* 45, 459–476.

1078 Miocic, J.M., Gilfillan, S.M.V., Roberts, J.J., Edlmann, K., McDermott, C.I.,
1079 Haszeldine, R.S., 2016. Controls on CO₂ storage security in natural reservoirs and

1080 implications for CO₂ storage site selection. *Int. J. Greenh. Gas Control* 51, 118–125.
1081 <https://doi.org/10.1016/j.ijggc.2016.05.019>

1082 Miocic, J.M., Johnson, G., Bond, C.E., 2019. Uncertainty in fault seal
1083 parameters: implications for CO₂ column height retention and storage capacity in
1084 geological CO₂ storage projects. *Solid Earth* 10, 951–967.
1085 <https://doi.org/10.5194/se-10-951-2019>

1086 Najafi-Marghmaleki, A., Tatar, A., Barati-Harooni, A., Mohebbi, A., Kalantari-
1087 Meybodi, M., Mohammadi, A.H., 2016. On the prediction of interfacial tension (IFT)
1088 for water-hydrocarbon gas system. *J. Mol. Liq.* 224, 976–990.
1089 <https://doi.org/10.1016/J.MOLLIQ.2016.10.083>

1090 Naylor, M., Wilkinson, M., Haszeldine, R.S., 2010. Calculation of CO₂
1091 column heights in depleted gas fields from known pre-production gas column
1092 heights. *Mar. Pet. Geol.* <https://doi.org/10.1016/j.marpetgeo.2010.10.005>

1093 Nordgard Bolas, H.M., Hermanrud, C., Teige, G.M.G., 2005. Seal capacity
1094 estimation from subsurface pore pressures. *Basin Res.* 17, 583–599.
1095 <https://doi.org/10.1111/j.1365-2117.2005.00281.x>

1096 Øren, P.-E., Bakke, S., 2003. Reconstruction of Berea sandstone and pore-
1097 scale modelling of wettability effects. *J. Pet. Sci. Eng.* 39, 177–199.
1098 [https://doi.org/10.1016/S0920-4105\(03\)00062-7](https://doi.org/10.1016/S0920-4105(03)00062-7)

1099 Pei, Y., Paton, D.A., Knipe, R.J., Wu, K., 2015. A review of fault sealing
1100 behaviour and its evaluation in siliciclastic rocks. *Earth-Science Rev.* 150, 121–138.
1101 <https://doi.org/10.1016/j.earscirev.2015.07.011>

1102 Peng, D.-Y., Robinson, D.B., 1976. A new two-constant equation of state.
1103 *Ind. Eng. Chem. Fundam.* 15, 59–64.

1104 Radke, C.J., Kovscek, A.R., Wong, H., 1992. A Pore-Level Scenario for the
1105 Development of Mixed Wettability in Oil Reservoirs, in: *SPE Annual Technical*
1106 *Conference and Exhibition*. Society of Petroleum Engineers.
1107 <https://doi.org/10.2118/24880-MS>

1108 Rajayi, M., Kantzas, A., 2011. Effect of Temperature and Pressure on
1109 Contact Angle and Interfacial Tension of Quartz/Water/Bitumen Systems. *J. Can.*
1110 *Pet. Technol.* 50, 61–67. <https://doi.org/10.2118/148631-PA>

1111 Ren, Q.Y., Chen, G.J., Yan, W., Guo, T.M., 2000. Interfacial tension of (CO₂
1112 + CH₄) + water from 298 K to 373 K and pressures up to 30 MPa. *J. Chem. Eng.*
1113 *Data* 45, 610–612. <https://doi.org/10.1021/je990301s>

1114 Rimstidt, J.D., Barnes, H.L., 1980. The kinetics of silica-water reactions.
1115 *Geochim. Cosmochim. Acta* 44, 1683–1699. [https://doi.org/10.1016/0016-](https://doi.org/10.1016/0016-7037(80)90220-3)
1116 [7037\(80\)90220-3](https://doi.org/10.1016/0016-7037(80)90220-3)

1117 Robert M. Sneider, J.S.S.G.W.B., Neasham, J.W., 1997. AAPG Memoir 67:
1118 Seals, Traps, and the Petroleum System. Chapter 1: Comparison of Seal Capacity
1119 Determinations: Conventional Cores vs. Cuttings 1–12.

1120 Schowalter, T.T., 1974. AAPG bulletin., AAPG Bulletin. American
1121 Association of Petroleum Geologists.

1122 Shipton, Z.K., Cowie, P.A., 2001. Damage zone and slip-surface evolution
1123 over μm to km scales in high-porosity Navajo sandstone, Utah. *J. Struct. Geol.* 23,
1124 1825–1844. [https://doi.org/10.1016/S0191-8141\(01\)00035-9](https://doi.org/10.1016/S0191-8141(01)00035-9)

1125 Shipton, Z.K., Evans, J.P., Robeson, K.R., Forster, C.B., Snelgrove, S.,
1126 2002. Structural heterogeneity and permeability in faulted eolian sandstone:
1127 Implications for subsurface modeling of faults. *AAPG Bull.* v 86, 863–883.

1128 Singh, K., Bijeljic, B., Blunt, M.J., 2016. Imaging of oil layers, curvature and
1129 contact angle in a mixed-wet and a water-wet carbonate rock. *Water Resour. Res.*
1130 52, 1716–1728. <https://doi.org/10.1002/2015WR018072>

1131 Sperrevik, S., Gillespie, P.A., Fisher, Q.J., Halvorsen, T., Knipe, R.J., 2002.
1132 Empirical estimation of fault rock properties. *Nor. Pet. Soc. Spec. Publ.* 11, 109–
1133 125. [https://doi.org/10.1016/S0928-8937\(02\)80010-8](https://doi.org/10.1016/S0928-8937(02)80010-8)

1134 Sutjiadi-Sia, Y., Jaeger, P., Eggers, R., 2008. Interfacial phenomena of
1135 aqueous systems in dense carbon dioxide. *J. Supercrit. Fluids* 46, 272–279.
1136 <https://doi.org/10.1016/J.SUPFLU.2008.06.001>

- 1137 Sutton, R.P., 2006. Oil system correlations. LAKE, LW Pet. Eng. Handbook.
1138 Soc. Pet. Eng. 1, 258–306.
- 1139 Tassone, D.R., Holford, S.P., Duddy, I.R., Green, P.F., Hillis, R.R., 2014.
1140 Quantifying Cretaceous–Cenozoic exhumation in the Otway Basin, southeastern
1141 Australia, using sonic transit time data: Implications for conventional and
1142 unconventional hydrocarbon prospectivity. Am. Assoc. Pet. Geol. Bull. 98, 67–117.
1143 <https://doi.org/10.1306/04011312111>
- 1144 Teasdale, J.P., Pryer, L.L., Stuart-Smith, P.G., Romine, K.K., Etheridge,
1145 M.A., Loutit, T.S., Kyan, D.M., 2003. Structural framework and basin evolution of
1146 Australia’s southern margin. APPEA J. 43, 13–37.
- 1147 Tenthorey, E., Dance, T., Cinar, Y., Ennis-King, J., Strand, J., 2014. Fault
1148 modelling and geomechanical integrity associated with the CO2CRC Otway 2C
1149 injection experiment. Int. J. Greenh. Gas Control 30, 72–85.
1150 <https://doi.org/10.1016/j.ijggc.2014.08.021>
- 1151 Tian Yi-Ling, T., Yan-Fan, X., Hong-Xu, Z., Xi-Jing, D., Xiao-Wen, R., Feng-
1152 Cai, Z., Yi-Ling, T., Yan-Fan, X., Hong-Xu, Z., Xi-Jing, D., Xiao-Wen, R., Feng-Cai,
1153 Z., 1997. Interfacial Tensions between Water and Non-polar Fluids at High
1154 Pressures and High Temperatures. Acta Physico-Chimica Sin. 13, 89–95.
1155 <https://doi.org/10.3866/PKU.WHXB19970120>
- 1156 Treiber, L.E., Owens, W.W., 1972. A Laboratory Evaluation of the Wettability
1157 of Fifty Oil-Producing Reservoirs. Soc. Pet. Eng. J. 12, 531–540.
1158 <https://doi.org/10.2118/3526-PA>
- 1159 Vavra, C.L., Kaldi, J.G., Sneider, R.M., 1992. Geological applications of
1160 capillary pressure: a review (1). Am. Assoc. Pet. Geol. Bull. 76, 840–850.
- 1161 Watson, M.N., Boreham, C.J., Tingate, P.R., 2004. Carbon dioxide and
1162 carbonate cements in the Otway Basin; implications for geological storage of carbon
1163 dioxide. APPEA J. 44, 703–720.
- 1164 Watson, M.N., Zwingmann, N., Lemon, N.M., Tingate, P.R., 2003. Onshore
1165 Otway Basin carbon dioxide accumulations: CO2-induced diagenesis in natural
1166 analogues for underground storage of greenhouse gas. APPEA J. 43, 637–653.

- 1167 Watts, N.L., 1987. Theoretical aspects of cap-rock and fault seals for single-
1168 and two-phase hydrocarbon columns. *Mar. Pet. Geol.* 4, 274–307.
1169 [https://doi.org/10.1016/0264-8172\(87\)90008-0](https://doi.org/10.1016/0264-8172(87)90008-0)
- 1170 Wiegand, G., Franck, E.U., 1994. Interfacial tension between water and non-
1171 polar fluids up to 473 K and 2800 bar. *Berichte der Bunsengesellschaft für Phys.*
1172 *Chemie* 98, 809–817. <https://doi.org/10.1002/bbpc.19940980608>
- 1173 Worden, R.H., Morad, S., 2000. Economic evaluation of a petroleum
1174 accumulation demands a Quartz cementation in oil field sandstones: a review of
1175 the key controversies. *Spec. Publs int. Ass. Sediment* 29, 1–20.
- 1176 Yielding, G., 2002. Shale Gouge Ratio — calibration by geohistory. *Nor. Pet.*
1177 *Soc. Spec. Publ.* 11, 1–15. [https://doi.org/10.1016/S0928-8937\(02\)80003-0](https://doi.org/10.1016/S0928-8937(02)80003-0)
- 1178 Yielding, G., Bretan, P., Freeman, B., 2010. Fault seal calibration: a brief
1179 review. *Geol. Soc. London, Spec. Publ.* 347, 243–255.
1180 <https://doi.org/10.1144/SP347.14>
- 1181 Yielding, G., Freeman, B., Needham, D.T., 1997. Quantitative fault seal
1182 prediction. *Am. Assoc. Pet. Geol. Bull.* 81, 897–917.
- 1183 Ziesch, J., Aruffo, C.M., Tanner, D.C., Beilecke, T., Dance, T., Henk, A.,
1184 Weber, B., Tenthorey, E., Lippmann, A., Krawczyk, C.M., 2017. Geological structure
1185 and kinematics of normal faults in the Otway Basin, Australia, based on quantitative
1186 analysis of 3-D seismic reflection data. *Basin Res.* 29, 129–148.
1187 <https://doi.org/10.1111/bre.12146>
- 1188 Ziesch, J., Aruffo, C.M., Tanner, D.C., Beilecke, T., Dance, T., Henk, A.,
1189 Weber, B., Tenthorey, E., Lippmann, A., Krawczyk, C.M., 2015. Geological structure
1190 and kinematics of normal faults in the Otway Basin, Australia, based on quantitative
1191 analysis of 3-D seismic reflection data. *Basin Res.* n/a-n/a.
1192 <https://doi.org/10.1111/bre.12146>